Multiscale fluid–particle thermal interaction in isotropic turbulence

M. Carbone[1,2], A. D. Bragg[2,†] and M. Iovieno[1]

[1]Dipartimento di Ingegneria Meccanica e Aerospaziale, Politecnico di Torino,
Corso Duca degli Abruzzi 24, 10129 Torino, Italy

[2]Department of Civil and Environmental Engineering, Duke University, Durham, NC 27708, USA

We use direct numerical simulations to investigate the interaction between the temperature field of a fluid and the temperature of small particles suspended in the flow, employing both one- and two-way thermal coupling, in a statistically stationary, isotropic turbulent flow. Using statistical analysis, we investigate this variegated interaction at the different scales of the flow. We find that the variance of the carrier flow temperature gradients decreases as the thermal response time of the suspended particles is increased. The probability density function (PDF) of the carrier flow temperature gradients scales with its variance, while the PDF of the rate of change of the particle temperature, whose variance is associated with the thermal dissipation due to the particles, does not scale in such a self-similar way. The modification of the fluid temperature field due to the particles is examined by computing the particle concentration and particle heat fluxes conditioned on the magnitude of the local fluid temperature gradient. These statistics highlight that the particles cluster on the fluid temperature fronts, and the important role played by the alignments of the particle velocity and the local fluid temperature gradient. The temperature structure functions, which characterize the temperature fluctuations across the scales of the flow, clearly show that the fluctuations of the carrier flow temperature increments are monotonically suppressed in the two-way coupled regime as the particle thermal response time is increased. Thermal caustics dominate the particle temperature increments at small scales, that is, particles that come into contact are likely to have very large differences in their temperatures. This is caused by the non-local thermal dynamics of the particles: the scaling exponents of the inertial particle temperature structure functions in the dissipation range reveal very strong multifractal behaviour. Further insight is provided by the flux of temperature increments across the scales. Altogether, these results reveal a number of non-trivial effects, with a number of important practical consequences.

Key words: multiphase and particle-laden flows

1. Introduction

The interaction between inertial particles and scalar fields in turbulent flows plays a central role in many natural problems, ranging from cloud microphysics (Pruppacher

† Email address for correspondence: andrew.bragg@duke.edu

& Klett 2010; Grabowski & Wang 2013) to the interactions between plankton and nutrients (De Lillo *et al.* 2014) and dust particle flows in accretion disks (Takeuchi & Lin 2002). In engineered systems, applications involve chemical reactors and combustion chambers, and more recently, microdispersed colloidal fluids, where the enhanced thermal conductivity due to particle aggregations can give rise to non-trivial thermal behaviour (Prasher *et al.* 2006; Momenifar *et al.* 2015), and which can be used in cooling devices for electronic equipment exposed to large heat fluxes (Das, Choi & Patel 2006).

In this work, we focus on the heat exchange between advected inertial particles and the fluid phase in a turbulent flow, with a parametric emphasis relevant to understanding particle–scalar interactions in cloud microphysics. Understanding the droplet growth in clouds requires one to characterize the interaction between water droplets and the humidity and temperature fields. A major problem is to understand how the interaction between turbulence, heat exchange, condensational processes and collisions can produce the rapid growth of water droplets that leads to rain initiation (Pruppacher & Klett 2010; Grabowski & Wang 2013). While the study of the transport of scalar fields and particles in turbulent flows are well established research areas in both theoretical and applied fluid dynamics (Taylor 1922; Kraichnan 1994), the characterization of the interaction between scalars and particles in turbulent flows is a relatively new topic (Bec, Homann & Krstulovic 2014), since the problem is hard to handle analytically, requires sophisticated experimental techniques and is computationally demanding.

When temperature differences inside the fluid are sufficiently small, the temperature field behaves almost like a passive scalar, that is, the fluid temperature is advected and diffused by the fluid motion but has negligible dynamical effect on the flow. Even in this regime, the statistical properties of the passive scalar field are significantly different from those of the underlying velocity field that advects it. Different regimes take place according to the Reynolds number and the ratio between momentum and scalar diffusivities (Shraiman & Siggia 2000; Warhaft 2000; Watanabe & Gotoh 2004).

Experiments, numerical simulations and analytical models show that a passive scalar field is always more intermittent than the velocity field, and passive scalars in turbulence are characterized by strong anomalous scaling (Holzer & Siggia 1994). This is due to the formation of ramp–cliff structures in the scalar field (Celani *et al.* 2000; Watanabe & Gotoh 2004): large regions in which the scalar field is almost constant are separated by thin regions in which the scalar abruptly changes. The regions in which the scalar mildly changes are referred to as Lagrangian coherent structures. The thin regions with large scalar gradient, where the diffusion of the scalar takes place, are referred to as fronts. It has been shown that the large-scale forcing influences the passive scalar statistics at small scales (Gotoh & Watanabe 2015). In particular, a mean scalar gradient forcing preserves universality of the statistics while a large-scale Gaussian forcing does not. However, the ramp–cliff structure was observed with different types of forcing, implying that this structure is universal to scalar fields in turbulence (Watanabe & Gotoh 2004; Bec *et al.* 2014). Moreover, recent measurements of atmospheric turbulence have shown that external boundary conditions, such as the magnitude and sign of the sensible heat flux, have a significant impact on the fluid temperature dynamics within the inertial range, while for the same scales the fluid velocity increments are essentially independent of these large-scale conditions (Zorzetto, Bragg & Katul 2018).

When a turbulent flow is seeded with inertial particles, the particles can sample the surrounding flow in a non-uniform and correlated manner (Toschi & Bodenschatz

2009). Particle inertia in a turbulent flow is measured through the Stokes number $St \equiv \tau_p/\tau_\eta$, which compares the particle response time to the Kolmogorov time scale. A striking feature of inertial particle motion in turbulent flows is that they spontaneously cluster even in incompressible flows (Maxey 1987; Wang & Maxey 1993; Bec *et al.* 2007; Ireland, Bragg & Collins 2016*a*). This clustering can take place across a wide range of scales (Bec *et al.* 2007; Bragg, Ireland & Collins 2015*a*; Ireland *et al.* 2016*a*), and the small-scale clustering is maximum when $St = O(1)$. A variety of mechanisms have been proposed to explain this phenomenon: when $St \ll 1$ the clustering is caused by particles being centrifuged out of regions of strong rotation (Maxey 1987; Chun *et al.* 2005), while for $St \geqslant O(1)$, a non-local mechanism generates the clustering, whose effect is related to the particles memory of its interaction with the flow along its path history (Gustavsson & Mehlig 2011; Bragg & Collins 2014*a*; Bragg, Ireland & Collins 2015*b*; Bragg *et al.* 2015*a*; Gustavsson & Mehlig 2016). Note that recent results on the clustering of settling inertial particles in turbulence have corroborated this picture, showing that strong clustering can occur even in a parameter regime where the centrifuge effect cannot be invoked as the explanation for the clustering, but it is caused by a non-local mechanism (Ireland, Bragg & Collins 2016*b*).

When particles have finite thermal inertia, they will not be in thermal equilibrium with the fluid temperature field, and this can give rise to non-trivial thermal coupling between the fluid and particles in a turbulent flow. A thermal response time τ_θ can be defined so that the particle thermal inertia is parameterized by the thermal Stokes number $St_\theta \equiv \tau_\theta/\tau_\eta$ (Zaichik, Alipchenkov & Sinaiski 2009). Since both the fluid temperature and particle phase-space dynamics depend upon the fluid velocity field, there can exist non-trivial correlations between the fluid and particle temperatures even in the absence of thermal coupling. Indeed, it was show by Bec *et al.* (2014) that inertial particles preferentially cluster on the fronts of the scalar field. Associated with this is that the particles preferentially sample the fluid temperature field, and when combined with the strong intermittency of temperature fields in turbulent flows, this can cause particles to experience very large temperature fluctuations along their trajectories.

Several works have considered aspects of the fluid–particle temperature coupling using numerical simulations. For example, Zonta, Marchioli & Soldati (2008) investigated a particle-laden channel flow, with a view to modelling the modification of heat transfer in micro-dispersed fluids. They considered both momentum and temperature two-way coupling and observed that, depending on the particle inertia, the heat flow at the wall can increase or decrease. Kuerten, van der Geld & Geurts (2011) considered a similar set-up with larger dispersed particles, and they observed a stronger modification of the fluid temperature statistics due to the particles. Zamansky *et al.* (2014, 2016) considered turbulence induced by buoyancy, where the buoyancy was generated by heated particles. They observed that the resulting flow is driven by thermal plumes produced by the particles. As the particle inertia was increased, the inhomogeneity and the effect of the coupling were enhanced in agreement with the fact that inertial particles tend to cluster on the scalar fronts. Kumar, Schumacher & Shaw (2014) examined how the spatial distribution of droplets is affected by large-scale inhomogeneities in the fluid temperature and supersaturation fields, considering the transition between homogeneous and inhomogeneous mixing. A similar flow configuration was also investigated by Götzfried *et al.* (2017).

Each of these studies was primarily focused on the effect of the inertial particles on the large-scale statistics of the fluid temperature field. However, the results of Bec

et al. (2014) imply that the effects of fluid–particle thermal coupling could be strong at the small scales, owing to the fact that they cluster on the fronts of the temperature field. Moreover, there is a need to understand and characterize the multiscale thermal properties of the particles themselves. In order to address these issues, we have conducted direct numerical simulations (DNS) to investigate the interaction between the scalar temperature field and the temperature of inertial particles suspended in a fluid, with one- and two-way thermal coupling, in statistically stationary, isotropic turbulence. Using statistical analysis, we probe the multiscale aspects of the problem and consider the particular ways that the inertial particles contribute to the properties of the fluid temperature field in the two-way coupled regime.

The paper is organized as follows. In §2 we present the physical model used in the DNS, and present the parameters in the system. In §3 the statistics of the fluid temperature and time derivative of the particle temperature are considered, which allow us to quantify the contributions to the thermal dissipation in the system from the fluid and particles. In §4 we consider the statistics of the fluid and particle temperatures. In §5 we consider the heat flux due to the particle motion conditioned on the local fluid temperature gradients in order to obtain insight into the details of the thermal coupling. In §6 we consider the structure functions of the fluid and particle temperature increments, along with their scaling exponents. In §7 we consider the probability density functions (PDFs) of the fluxes of fluid and particle temperature increments across the scales of the flow. Finally, concluding remarks are given in §8.

2. The physical model

In this section we present the governing equations of the physical model which will be solved numerically to simulate the thermal coupling and behaviour of a particle-laden turbulent flow.

2.1. *Fluid phase*

We consider a statistically stationary, homogeneous and isotropic turbulent flow, governed by the incompressible Navier–Stokes equations. The turbulent velocity field advects the fluid temperature field (assumed a passive scalar), together with the inertial particles. In this study, we account for two-way thermal coupling between the fluid and particles, but only one-way momentum coupling. Therefore, the governing equations for the fluid phase are

$$\boldsymbol{\nabla} \cdot \boldsymbol{u} = 0, \tag{2.1a}$$

$$\partial_t \boldsymbol{u} + \boldsymbol{u} \cdot \boldsymbol{\nabla} \boldsymbol{u} = -\frac{1}{\rho_0} \boldsymbol{\nabla} p + \nu \nabla^2 \boldsymbol{u} + \boldsymbol{f}, \tag{2.1b}$$

$$\partial_t T + \boldsymbol{u} \cdot \boldsymbol{\nabla} T = \kappa \nabla^2 T - C_T + f_T. \tag{2.1c}$$

Here $\boldsymbol{u}(\boldsymbol{x}, t)$ is the velocity of the fluid, $p(\boldsymbol{x}, t)$ is the pressure, ρ_0 is the density of the fluid, ν is its kinematic viscosity, $T(\boldsymbol{x}, t)$ is the temperature of the fluid and κ is the thermal diffusivity. The ratio between the momentum diffusivity ν and the thermal diffusivity κ defines the Prandtl number $Pr \equiv \nu/\kappa$. In this work, we consider $Pr = 1$, leaving further exploration of its effect on the system to future work. The $\boldsymbol{f}$ and f_T terms in (2.1b) and (2.1c) represent the external forcing, and C_T is the thermal feedback of the particles on the fluid temperature field, that is, the heat exchanged per unit time and unit volume between the fluid and particles at position $\boldsymbol{x}$.

When the forcing is confined to sufficiently large scales, it is assumed that the details of the forcing do not influence the small-scale dynamics. Previous experimental evidence seems to confirm this (Sreenivasan 1996), leading to a universal behaviour of the small scales. However, recent studies (Gotoh & Watanabe 2015) pointed out that this hypothesis of universality is partially violated by the advected scalar fields, whose inertial range statistics exhibit sensitivity to the details of the imposed forcing. Since we aim to characterize temperature and temperature gradient fluctuations in the dissipation range for different inertias of the suspended particles, we employ a forcing that imposes the same total dissipation rate for all the simulations. This produces results which can be meaningfully compared for different parameters of the suspended particles, since the response of the system to the same injected thermal power can be examined. Therefore, we employ the large-scale forcing (Kumar, Schumacher & Shaw 2013; Kumar *et al.* 2014),

$$\hat{\boldsymbol{f}}(\boldsymbol{k}, t) = \varepsilon \frac{\hat{\boldsymbol{u}}(\boldsymbol{k}, t)}{\displaystyle\sum_{\boldsymbol{k}_f \in \mathcal{K}_f} \|\hat{\boldsymbol{u}}(\boldsymbol{k}_f, t)\|2} \delta_{\boldsymbol{k}, \boldsymbol{k}_f}, \quad \hat{f}_T(\boldsymbol{k}, t) = \chi \frac{\hat{T}(\boldsymbol{k}, t)}{\displaystyle\sum_{\boldsymbol{k}_f \in \mathcal{K}_f} |\hat{T}(\boldsymbol{k}_f, t)|2} \delta_{\boldsymbol{k}, \boldsymbol{k}_f}, \quad (2.2a,b)$$

in the wavenumber space. A hat indicates the Fourier transform and $\boldsymbol{k}_f$ is the wavenumber which here belongs to the set of forced wavenumbers, $\mathcal{K}_f = \{\boldsymbol{k}_f : \|\boldsymbol{k}_f\| = k_f\}$; ε and χ are the imposed dissipation rates of velocity and temperature variance, respectively. This employed forcing scheme thus allows us to control the overall dissipation rate and, therefore, to control the Stokes number.

The values of the parameters relative to the fluid flow employed in the simulations are given in table 1. Time-averaged energy and temperature spectra, in the absence of particle thermal feedback, are shown in figure 1(*a*).

2.2. *Particle phase*

We consider rigid, point-like particles which are heavy with respect to the fluid, and small with respect to any scale of the flow. In particular, the particle density ρ_p is much larger than the fluid density $\rho_p \gg \rho_0$, and the particle radius r_p is much smaller than the Kolmogorov length scale $r_p \ll \eta$. With these assumptions (and neglecting gravity) the particle acceleration is described by the Stokes drag law. Analogously, the rate of change of the particle temperature is described by Newton's law for the heat conduction

$$\frac{\mathrm{d}\boldsymbol{x}_p}{\mathrm{d}t} \equiv \boldsymbol{v}_p, \quad (2.3a)$$

$$\frac{\mathrm{d}\boldsymbol{v}_p}{\mathrm{d}t} = \frac{\boldsymbol{u}(\boldsymbol{x}_p, t) - \boldsymbol{v}_p}{\tau_p}, \quad (2.3b)$$

$$\frac{\mathrm{d}\theta_p}{\mathrm{d}t} = \frac{T(\boldsymbol{x}_p, t) - \theta_p}{\tau_\theta}. \quad (2.3c)$$

Here, $\tau_p \equiv 2\rho_p r_p^2/(9\rho_0 \nu)$ is the particle momentum response time, $\tau_\theta \equiv \rho_p c_p r_p^2/(3\rho_0 c_0 \kappa)$ is the particle thermal response time, c_p is the particle heat capacity and c_0 is the fluid heat capacity at constant pressure. The Stokes number is defined as $St \equiv \tau_p/\tau_\eta$, and the thermal Stokes number is defined as $St_\theta \equiv \tau_\theta/\tau_\eta$, where τ_η is the Kolmogorov time scale.

We consider nine values of St_θ and three values of St in order to explore the behaviour of the system over a range of parameter values. Since we are accounting

Kinematic viscosity	ν	0.005
Prandtl number	Pr	1
Velocity fluctuation dissipation rate	ε	0.27
Temperature fluctuation dissipation rate	χ	0.1
Kolmogorov time scale	τ_η	0.136
Kolmogorov length scale	η	0.0261
Taylor micro-scale	λ	0.498
Integral length scale	ℓ	1.4
Root mean square velocity	u'	0.88
Kolmogorov velocity scale	u_η	0.192
Small-scale temperature	T_η	0.117
Taylor Reynolds number	Re_λ	88
Integral-scale Reynolds number	Re_l	244
Forced wavenumber	k_f	$\sqrt{2}$
Number of Fourier modes	N	128 (3/2)
Resolution	$N\eta/2$	1.67

TABLE 1. Flow parameters for the numerical simulations in this study. Dimensional parameters are non-dimensionalized into arbitrary code units. The characteristic parameters of the fluid flow are defined from its energy spectrum $E(k) \equiv \int_{\|\boldsymbol{k}\|=k} \|\hat{\boldsymbol{u}}(\boldsymbol{k})\|^2 \, \mathrm{d}\boldsymbol{k}/2$. The dissipation rate of turbulent kinetic energy is $\varepsilon \equiv 2\nu \int k^2 E(k) \, \mathrm{d}k$. The Kolmogorov length $\eta \equiv (\nu^3/\varepsilon)^{1/4}$, time scale $\tau_\eta \equiv (\nu/\varepsilon)^{1/2}$ and velocity scale $u_\eta \equiv \eta/\tau_\eta$. The Taylor micro-scale is $\lambda \equiv u'/\sqrt{\langle|\boldsymbol{\nabla u}|^2\rangle}$. The root mean square velocity is $u' \equiv \sqrt{(2/3) \int E(k) \, \mathrm{d}k}$ and the integral length scale $\ell \equiv \pi/(2u'^2) \int E(k)/k \, \mathrm{d}k$. Similarly, the spectrum, root mean square value and dissipation rate of the scalar field are $E_T(k) \equiv \int_{\|\boldsymbol{k}\|=k} |\hat{T}(\boldsymbol{k})|^2 \, \mathrm{d}\boldsymbol{k}/2$, $T' \equiv \sqrt{2 \int E_T(k) \, \mathrm{d}k}$, $\chi_f \equiv 2\kappa \int k^2 E_T(k) \, \mathrm{d}k$. The small-scale temperature is determined by the viscosity and dissipation rate: $T_\eta \equiv \sqrt{\chi \tau_\eta}$. Since the Prandtl number is unitary the small scales of the scalar and the velocity field are of the same order.

for thermal coupling, each combination of St_θ and St must be simulated separately, and when combined with the large number of particles in the flow domain, the set of simulations require considerable computational resources. Therefore, in the present study we restrict attention to $Re_\lambda = 88$, but future explorations should consider larger Re_λ in order to explore the behaviour when there exists a well-defined inertial range in the flow.

In order to obtain deeper insight into the role of the two-way thermal coupling, we perform simulations with (denoted by S1) and without (denoted by S2) the thermal coupling. The particle parameters employed in the simulations are given in table 2. The second-order longitudinal structure functions of the particle velocity are shown in figure 1(b) for all the Stokes numbers investigated.

2.3. *Thermal coupling*

In the two-way thermal coupling regime, the thermal energy contained in the fluid is finite with respect to the thermal energy of the particles, therefore, when heat flows from the fluid to the particle the fluid loses thermal energy at the particle position. Due to the point-mass approximation, the feedback from the particles on the fluid temperature field is a superposition of Dirac delta functions, centred on the particles. Hence the coupling term in (2.1c) is given by

Particle phase volume fraction	ϕ	0.0004
Particle to fluid density ratio	ρ_p/ρ_0	1000
Particle back reaction	C_T	S1: included; S2: neglected
Stokes number	St	0.5; 1; 3
Thermal Stokes number	St_θ	0.2; 0.6; 1; 1.5; 2; 3; 4; 5; 6
Number of particles	N_P	12 500 992; 4 419 584; 847 872

TABLE 2. Particle parameters in dimensionless code units. The Stokes number is $St \equiv \tau_p/\tau_\eta$ and the thermal Stokes number $St_\theta \equiv \tau_\theta/\tau_\eta$; the particle response times are defined in the text. In the simulations, St_θ is varied by varying the particle heat capacity. The different combinations of St and St_θ are simulated including the two-way thermal coupling (simulations S1) and neglecting it (simulations S2).

$$C_T(\boldsymbol{x}, t) = \frac{4}{3}\pi \frac{\rho_p}{\rho_0}\frac{c_p}{c_0} r_p^3 \sum_{p=1}^{N_P} \frac{\mathrm{d}\theta_p}{\mathrm{d}t}\delta(\boldsymbol{x} - \boldsymbol{x}_p). \tag{2.4}$$

2.4. *Validity and limitations of the model*

The physical model in §§ 2.1–2.3, is normally referred to as point-particle model. The two-way thermal coupling regime is considered, that is, the particles can affect the fluid temperature field while the direct particle–particle thermal interaction is neglected. Previous estimations (Elghobashi 1991) have shown that particle–particle interactions become relevant at average volume fractions ϕ exceeding 10^{-3}. In this work, the volume fraction lies in the two-way coupling regime and the average distance between particles exceeds the particle diameter by an order of magnitude. In our simulations $\phi = 4 \times 10^{-4}$, which is small enough to neglect particle collisions, but large enough for two-way momentum coupling between the particles and fluid to be important (e.g. Elghobashi 1994). Nevertheless, we ignore two-way momentum coupling in the present study. The motivation is that including both two-way momentum and two-way thermal coupling introduces too many competing effects that would compound a thorough understanding of the problem. We therefore employ a reductionistic approach, seeking first to understand the role of two-way thermal coupling in the absence of momentum coupling, and then in a future study will explore their combined effects. Even aside from this methodological point, the results still have physical relevance since the thermal relaxation time is often larger than the momentum relaxation time in many particle-laden flows. For example, St_θ/St ranges from 2 to 6 for many liquid droplets in air ($\approx$4 for water droplets in air). Therefore thermal feedback can be more relevant to the thermal balance than momentum feedback on momentum balance. This is confirmed by the analysis of the effect of momentum coupling and elastic collisions on the temperature statistics, presented in appendix A. An additional set of simulations shows that, in the range of parameters considered in this work, both phenomena have a minimal effect.

The numerical solution of (2.1*b,c*) and (2.3) is considered a DNS, insofar as the Kolmogorov scale is resolved (Kuerten 2016), even though the details of the flow near the surface of each particle are not resolved. This point-particle simplification is formally valid for particles which are smaller than the smallest active scale in the flow, the Kolmogorov microscale (Toschi & Bodenschatz 2009). When the particle Reynolds number (based on the slip velocity between the particle and the local fluid)

is small, the effect of the stresses on the particle can be described using a Stokes drag force (Maxey & Riley 1983). Under an analogous set of conditions, the heat transfer between the particle and the fluid is a diffusive process, that has a time scale r_p^2/κ. For small point-like particles, this time scale is much smaller than the Kolmogorov time scale, so that the heat transfer is a quasi-steady process which leads to the Newton-like equation for heat transfer in (2.4) (Zonta *et al.* 2008; Bec *et al.* 2014). In this work, the ratio between the particle radius r_p and the Kolmogorov scale η is well below 0.1 for $St = 0.5$ and $St = 1$ and approximately 0.1 at $St = 3$. Therefore finite size effects are negligible up to $St = 1$, while there may be small errors for $St = 3$. The impact of these small errors should be quantified in a future work using a more sophisticated model that resolves the flow around the particle surface. Also the fluid continuity equation should be in principle modified, due to the volume occupied by inertial particles. However, the error introduced in the continuity equation, proportional to the rate of change of the local volume fraction, is of the same order as the error introduced by other approximations in the model which are quite small.

In the point-mass Eulerian–Lagrangian model here employed, the fluid temperature in (2.3c) should be understood as the temperature of the carrier fluid flow without the local effect of the disturbance due to the presence of the particles (Boivin, Simonin & Squires 1998). Neglecting this disturbance is justified for particles with a diameter much smaller than the Kolmogorov scale and much smaller than the grid spacing. In the case of two-way momentum coupling, the error introduced by neglecting the disturbance can be estimated to be less than 10 % for the particle parameters we are considering (Horwitz & Mani 2016). A similar estimation is expected for the fluid temperature disturbance due to the particle, since the equations for the particle velocity and temperature are analogous. At the largest simulated Stokes number, $St = 3$, the same estimation indicates that an error of approximately 15 % can be introduced. Therefore, the error is larger for this case, though certainly a sub-leading effect. Some simplified, efficient ways to compute the effect of the particle disturbance are available for the two-way momentum coupling (Horwitz & Mani 2016), but equivalent models for the thermal coupling problem are not well developed or tested. Given this, and the fact that for our small particles the corrections due to the disturbance terms would be sub-leading, it is justified to neglect their effect as a first approximation for understanding this complex problem.

We also emphasize that the statistics of the fluid temperature field presented in the paper refer to the carrier, resolved, temperature field, with the disturbance temperature field produced by the particles neglected. The actual (or total) temperature field is the superposition of the carrier temperature field and the disturbance induced by the particles. In the limit of large scale separation between the particle size and Kolmogorov scale and in the dilute regime, the disturbance field produced by the particle can be determined analytically and so the statistics of the actual temperature field can be reconstructed knowing the resolved carrier flow and the analytic solution for the particle temperature disturbance field. This aspect is discussed in appendix B.

Summarizing, because of the marked scale separation between the particle size and the Kolmogorov scale, $r_p \ll \eta$, and low particle volume fraction, $\phi \ll 1$, which are the conditions explored in our study, the point-particle method provides a good first approximation to the complex problem under consideration. The statistics for the temperature field reported in the paper refer to the carrier temperature field, in which the near-particle temperature changes are excluded, while the statistics of the actual temperature field can be recovered *a posteriori* on the basis of the modelling hypothesis. Future work should explore the problem using methods where

the flow around the particle is resolved, referred to as FRDNS (fully resolved DNS) (Boivin *et al.* 1998; Gualtieri *et al.* 2015). However, even with currently available high performance computational resources, FRDNS is limited to a small number of particles, making it unfeasible at present to explore the problem of interest in this work (Botto & Prosperetti 2012).

2.5. *Numerical method*

We perform direct numerical simulation of incompressible, statistically steady and isotropic turbulence on a tri-periodic cubic domain. Equations (2.1*a*), (2.1*b*) and (2.1*c*) are solved by means of the pseudo-spectral Fourier method for the spatial discretization. The 3/2 rule is employed for dealiasing (Canuto *et al.* 1988), so that the maximum resolved wavenumber is $k_{max} = N/2$. The required Fourier transforms are executed in parallel using the P3DFFT library (Pekurovsky 2012). Forcing is applied to a single scale, that is to all wavevectors satisfying $\|\boldsymbol{k}\|^2 = k_f$, with $k_f = 2$, and the equations for the fluid velocity and temperature Fourier coefficients are evolved in time by means of a second-order Runge–Kutta exponential integrator (Hochbruck & Ostermann 2010). This method has been preferred to the standard integrating factor because of its higher accuracy and, above all, because of its consistency. Indeed, in order to obtain an accurate representation of small-scale temperature fluctuations, it is critical that the numerical solution conserves thermal energy. The same time integration scheme is used to solve particle equations (2.3*a*), (2.3*b*) and (2.3*c*), thus providing overall consistency, since the system formed by fluid and particles is evolved in time as a whole.

The fluid velocity and temperature are interpolated at the particle position by means of fourth-order B-spline interpolation. The interpolation is implemented as a backward non-uniform fast Fourier transform (NUFFT) with B-spline basis: the fluid field is projected onto the B-spline basis in Fourier space through a deconvolution, then transformed into the physical space by means of a inverse fast Fourier transform (FFT). A convolution provides the interpolated field at particle positions (Beylkin 1995). Since B-splines have a compact support in physical space and deconvolution in Fourier space reduces to a division, this provide an efficient way to obtain high-order interpolation. This guarantees smooth and accurate interpolation and its efficient implementation is suitable for pseudo-spectral methods (van Hinsberg *et al.* 2012). The coupling term (2.4) has to be projected on the Cartesian grid used to represent the fields. This is performed by means of the forward NUFFT with B-spline basis (Beylkin 1995). Briefly, the algorithm works as follows (Carbone & Iovieno 2018). The convolution of the distribution $C_T(\boldsymbol{x}, t)$ with the B-spline polynomial basis $B(\boldsymbol{x})$ is computed in physical space, so that it can be effectively represented on the Cartesian grid

$$\widetilde{C}_T(\boldsymbol{x}, t) = C_T * B = \frac{4}{3}\pi \frac{\rho_p}{\rho_0} \frac{c_p}{c_0} r_p^3 \sum_{p=1}^{N_P} \frac{\mathrm{d}\theta_p}{\mathrm{d}t} B(\boldsymbol{x} - \boldsymbol{x}_p). \tag{2.5}$$

The smoothed field $\widetilde{C}_T$ is transformed by means of a FFT giving $\mathcal{F}[\widetilde{C}_T]$ in Fourier space. Finally, the convolution with the B-spline is removed in Fourier space,

$$\widehat{C}(\boldsymbol{k}, t) = \frac{\mathcal{F}[C_T * B]}{\mathcal{F}[B]} = \frac{\mathcal{F}[\widetilde{C}_T]}{\mathcal{F}[B]}. \tag{2.6}$$

Since the convolution is removed in Fourier space, increasing the order of B-spline provides higher accuracy, without introducing non-locality, even if the number of grid points influenced by each particle becomes larger in the preliminary convolution. A fourth-order B-spline polynomial is employed in these simulations and a test with the same forcing, same parameters, with a larger resolution (256^3 Fourier modes) confirmed the grid independence of the results. Also, the backward and forward transformations are symmetric, that guarantees energy conservation (Sundaram & Collins 1996). A detailed description and assessment of the NUFFT in the framework of particles in turbulence can be found in Carbone & Iovieno (2018).

3. Characterization of the thermal dissipation rate

In the flow under consideration, the total dissipation rate of the temperature field χ is constant due to the forcing term f_T. The total dissipation has a contribution from the carrier fluid and particle phases and is given by

$$\chi = \kappa \langle \|\boldsymbol{\nabla} T\|^2 \rangle + \frac{\phi}{\tau_\theta} \frac{\rho_p c_p}{\rho_0 c_0} \langle (T(\boldsymbol{x}_p, t) - \theta_p)^2 \rangle. \tag{3.1}$$

An analogous balance was derived for the kinetic energy dissipation rate (Sundaram & Collins 1996). It is worth noting that, in practice, the sense of the bracket operator is not strictly the same for the two terms: one is computed as spatial and time average, while the other is computed as time average over the set of particles. We indicate with χ_f the dissipation due to the fluid temperature gradient and with χ_p the dissipation due to the particles, the two terms on the right-hand side of (3.1), so that $\chi = \chi_f + \chi_p$. Note that both contributions to the dissipation rate are proportional to the kinematic thermal conductivity of the fluid since $\tau_\theta \propto 1/\kappa$, and hence both the dissipation mechanisms are due to molecular diffusivity. By inserting the definition of the particle thermal relaxation time into (3.1), it is possible to rewrite it as

$$\chi = \kappa \left[\langle \|\boldsymbol{\nabla} T\|^2 \rangle + 3\phi \left\langle \left(\frac{T(\boldsymbol{x}_p, t) - \theta_p}{r_p} \right)^2 \right\rangle \right], \tag{3.2}$$

which evidences that the temperature disturbance induced by the particle has a length scale of the order of the particle radius.

The portion of temperature fluctuations dissipated by the two different mechanisms depends on the statistics of the differences between the particle and local carrier flow temperatures. In the limit $St_\theta \to 0$ we have $T(\boldsymbol{x}_p, t) = \theta_p$, such that all of the dissipation is associated with the fluid. In the general case, the statistics of $T(\boldsymbol{x}_p, t) - \theta_p$ depend not only on St_θ, but also implicitly upon St, with the statistics of $T(\boldsymbol{x}_p, t)$ depending on the spatial clustering of the particles. This coupling between the particle momentum and temperature dynamics can lead to non-trivial effects of particle inertia on χ_p. Physically, the overall dissipation rate of the temperature field is due to the gradients of the total temperature gradients, which is the superposition of the carrier temperature field and the near-particle temperature field, with the total temperature equal to the particle temperature at the particle surface. However, the point-particle model separates the dissipation rate due to the carrier, resolved, temperature field χ_f and the dissipation rate due to the suspended particles χ_p. This is allowed because of the marked scale separation between the smallest scale of the carrier field, that is the Kolmogorov scale η, and the scale of the gradients induced by the suspended particles, that is the particle size r_p, with $r_p \ll \eta$. This is detailed in appendix B, in which the relation between the moments of the carrier temperature field gradient and the actual temperature field gradient is also discussed.
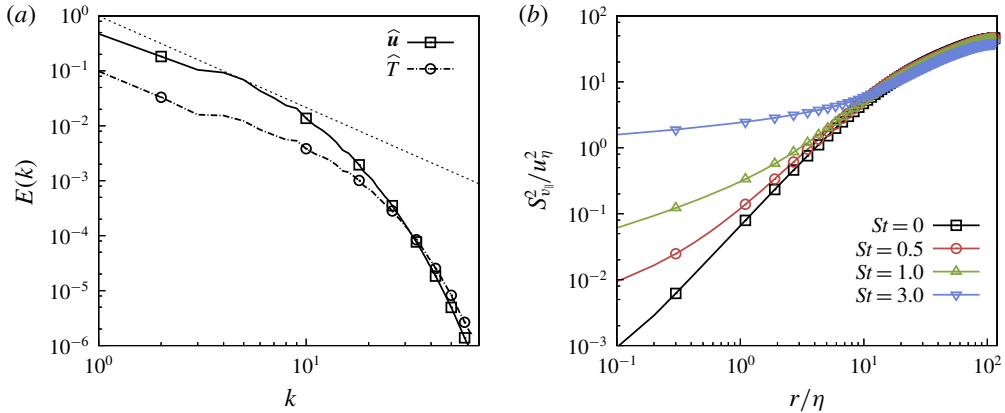
FIGURE 1. (Colour online) (*a*) Three-dimensional energy spectrum of the fluid velocity field (open squares) and temperature field (open circles). The temperature field is computed without any feedback from the particles on the fluid flow (simulations S2). (*b*) Second-order longitudinal structure functions of the particle velocity for various Stokes numbers.
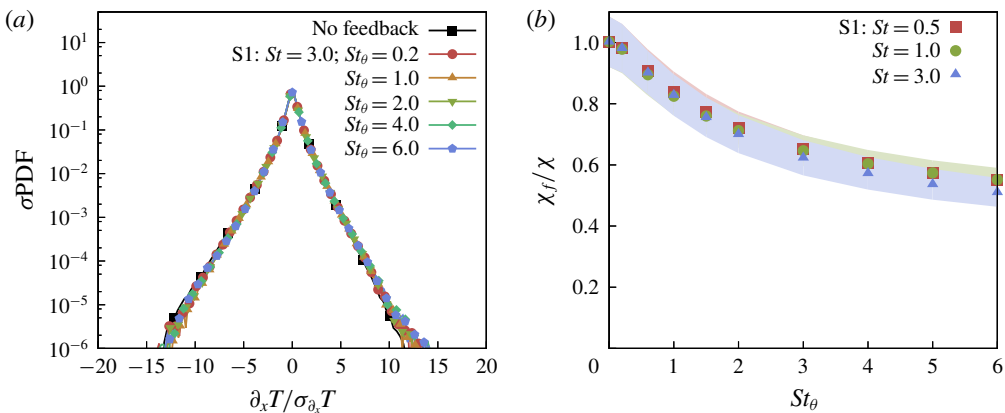

FIGURE 2. (Colour online) PDF of the carrier flow temperature gradient $\partial_x T$ from simulations S1, at $St = 3$, for various St_θ (*a*,*b*) dissipation rate, χ_f, of the fluid temperature fluctuations, for different St as a function of St_θ. The filled lines indicate the maximum deviations of the dissipation rate occurred in the time interval used to compute averages.

3.1. *Thermal dissipation due to the carrier temperature gradients*

Since the flow is isotropic, χ_f is given by

$$\chi_f = 3\kappa \langle (\partial_x T)^2 \rangle. \tag{3.3}$$

We consider fixed Reynolds number and $Pr = 1$, thus κ is the same in all the presented simulations, and so $\langle (\partial_x T)^2 \rangle$ fully characterizes χ_f. Moreover, given the expected structure of the field $\partial_x T$, it is instructive to consider its full probability density function (PDF), in addition to its moments in order to know how different regions of the flow contribute to the average dissipation rate χ_f.

Figure 2(*a*) shows the normalized PDFs of $\partial_x T$ for $St = 3$, for various St_θ, where the PDFs are normalized using the standard deviation of the distribution, $\sigma_{\partial_x T}$. The

distribution is almost symmetric and it displays elongated exponential tails. The largest temperature gradients exceed the standard deviation by an order of magnitude (Overholt & Pope 1996). Remarkably, the shape of the PDF shows a very weak dependence on St and St_θ, over all the considered range of these parameters, such that the PDF shape scales with $\sigma_{\partial_x T}$. Consistently, the kurtosis of the fluid temperature gradients distribution is approximately constant, which confirms that the fluid temperature gradient PDF is approximately self-similar.

The variance of the resolved fluid temperature gradient is proportional to the actual dissipation rate of the temperature fluctuation χ_f (the proportionality factor being 3κ, the same in all the simulations). In contrast to the PDF shape, the suspended particles have a strong impact on χ_f, as shown in figure 2. As St_θ is increased, χ_f decreases. However, this is mainly due to the fact that as St_θ is increased, χ_p increases, and so χ_f must decrease since $\chi = \chi_f + \chi_p$ is fixed. The influence of the Stokes number on χ_f is very small in the range of parameters considered.

3.2. *Thermal dissipation due to the particle dynamics*

The dissipation rate due to the particles, χ_p, depends on the difference between the particle temperature and the fluid temperature at the particle position,

$$\chi_p = 3\kappa\phi \left\langle \left(\frac{T(\boldsymbol{x}_p, t) - \theta_p}{r_p} \right)^2 \right\rangle. \tag{3.4}$$

For notational simplicity, we define $\varphi_p \equiv \sqrt{3\phi}(T(\boldsymbol{x}_p, t) - \theta_p)/r_p$. When φ_p is normalized by its standard deviation, we can relate this to the rate of change of the particle temperature using (2.3c)

$$\frac{\dot{\theta}_p}{\sigma_{\dot{\theta}_p}} = \frac{\varphi_p}{\sigma_{\varphi_p}}. \tag{3.5}$$

The normalized PDF of $\dot{\theta}_p$ for $St = 1$ and $St = 3$, and for various St_θ is shown in figure 3. Figure 3(a) shows the normalized PDF of $\dot{\theta}_p$, for $St = 1$ for the set of simulations S1, in which the two-way thermal coupling is taken to account. Figure 3(b) shows the corresponding results for simulations S2, in which the two-way thermal coupling is neglected. The normalized PDF of $\dot{\theta}_p$ for $St = 3$, with and without the two-way thermal coupling, is shown in figure 3(c,d).

In contrast to the fluid temperature gradient PDFs, the shape of the PDF of $\dot{\theta}_p$ is not self-similar with respect to its variance. As St_θ is increased, the normalized PDF becomes narrower. This is due to the fact that as St_θ is increased, the particles respond more slowly to changes in the fluid temperature field, analogous to the 'filtering' effect for inertial particle velocities in turbulence (Salazar & Collins 2012; Ireland *et al.* 2016a). The PDF shapes are mildly affected by St, and for larger St_θ, extreme fluid temperature–particle temperature differences are suppressed when the two-way thermal coupling is neglected.

The variance of $\dot{\theta}_p$ is proportional to the particle dissipation rate χ_p,

$$\langle \dot{\theta}_p^2 \rangle = \left\langle \frac{(T(\boldsymbol{x}_p, t) - \theta_p)^2}{\tau_\theta^2} \right\rangle = \frac{r_p^2 \chi_p}{3\kappa\phi\tau_\theta^2}, \tag{3.6}$$

and the results for this are shown in figure 3(e), for various St and St_θ, and for simulations S1 and S2. The results show that as St_θ is increased, χ_p increases. This
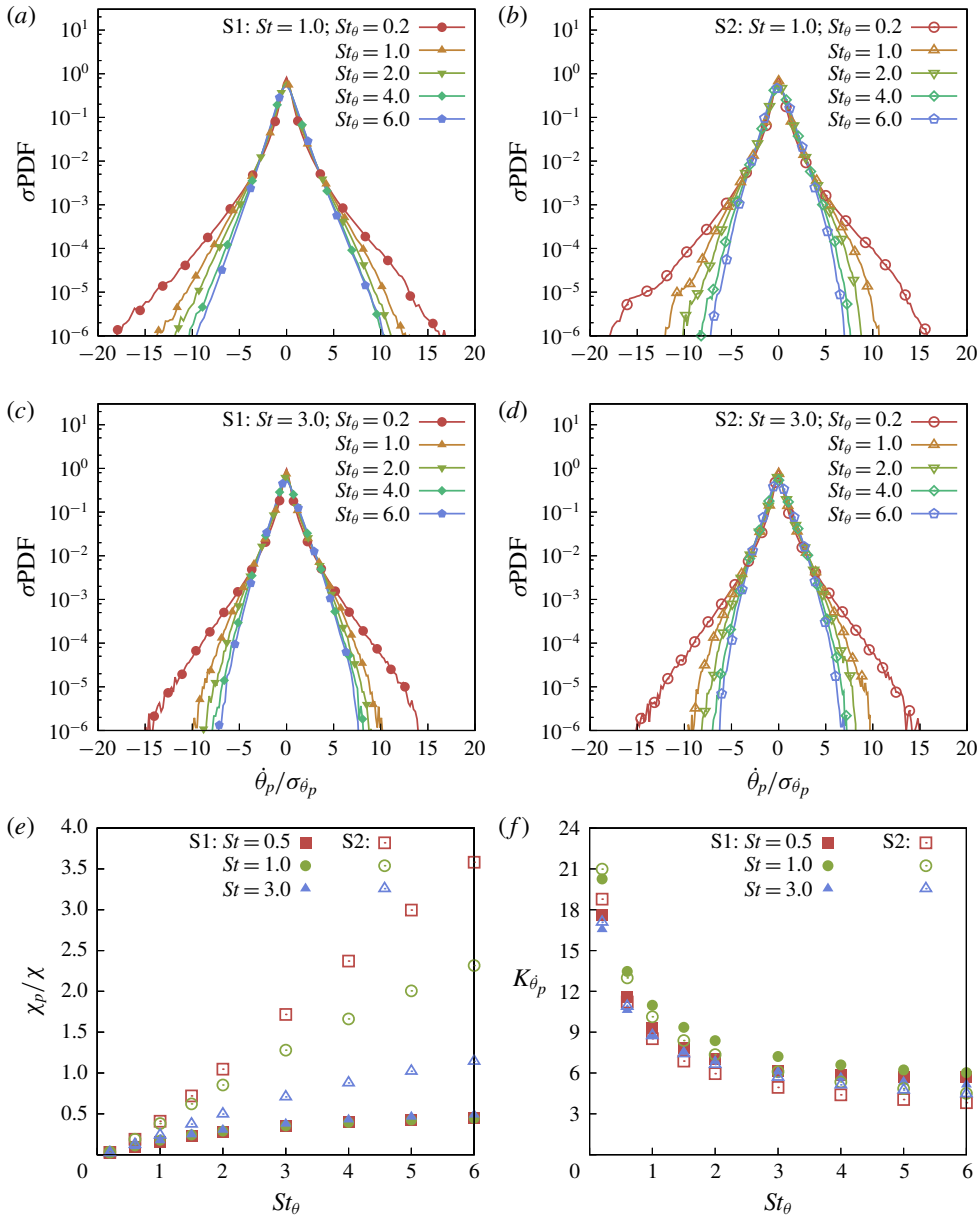
FIGURE 3. (Colour online) PDF of $\dot{\theta}_p$ for $St = 1$ (*a,b*) and $St = 3$ (*c,d*), and for various St_θ. Panels (*a–c*) are from simulations S1, in which the two-way thermal coupling is considered, while panels (*b–d*) are from simulations S2, in which the two-way coupling is neglected. (*e*) Dissipation rate χ_p of the temperature fluctuations due to the particles, for different St as a function of St_θ. (*f*) Kurtosis of the PDF of $\dot{\theta}_p$.

is mainly because as St_θ is increased, the thermal time correlation of the particle increases, and the particle temperature depends strongly on its encounter with the fluid temperature field along its trajectory history for times up to $O(\tau_\theta)$ in the past. As a result, the particle temperature can differ strongly from the local carrier flow

temperature. The results also show that χ_p is dramatically suppressed when two-way thermal coupling is accounted for. One reason for this is that as shown earlier, two-way thermal coupling leads to a suppression in the fluid temperature gradients. As these gradients are suppressed, the fluid temperature along the particle trajectory history differs less from the local carrier flow temperature than it would have in the absence of two-way thermal coupling, and as a result χ_p is decreased.

The results for kurtosis of $\dot{\theta}_p$, as a function of St_θ and for various St are shown in figure 3(*f*). The results show that the kurtosis decreases with increasing St_θ. This is mainly due to the filtering effect mentioned earlier, wherein as St_θ is increased, the particles are less able to respond to rapid fluctuations in the fluid temperature along their trajectory. Further, the kurtosis is typically larger when the two-way thermal coupling is taken into account (simulations S1), and is maximum for $St = 1$. This is due to the particle clustering on the fronts of the fluid temperature field, as will be discussed in § 5.

Our results for the PDF of $\dot{\theta}_p$ and its moments differ somewhat from those in Bec *et al.* (2014). This is in part due to the difference in the forcing methods employed by Bec *et al.* (2014) and that in our study. The solution of (2.3*c*) may be written as (Bec *et al.* 2014)

$$\langle \dot{\theta}_p^2 \rangle = \frac{1}{2\tau_\theta^3} \int_0^\infty \langle (\delta_t T_p(t))^2 \rangle \exp\left(-\frac{t}{\tau_\theta}\right) \, \mathrm{d}t, \tag{3.7}$$

where $\delta_t T_p(t) \equiv T(\boldsymbol{x}_p(t), t) - T(\boldsymbol{x}_p(0), 0)$. In the regime $St_\theta \ll 1$, the exponential in (3.7) decays very fast in time so that the main contribution to the integral comes from $\delta_t T_p$ for infinitesimal t, with $\delta_t T_p \sim t^n$ for $t \to 0$. Substituting $\delta_t T_p \sim t^n$ into (3.7) we obtain the leading-order behaviour

$$\langle \dot{\theta}_p^2 \rangle \sim \frac{1}{2\tau_\theta^3} \int_0^\infty t^{2n} \exp\left(-\frac{t}{\tau_\theta}\right) \, \mathrm{d}t \sim St_\theta^{2n-2}, \quad St_\theta \ll 1. \tag{3.8}$$

Bec *et al.* (2014) used a white in time forcing for the fluid scalar field, giving $n = 1/2$, and yielding $\langle \dot{\theta}_p^2 \rangle \sim St_\theta^{-1}$ for $St_\theta \ll 1$. However, the forcing scheme that we have employed generates a field $T(\boldsymbol{x}, t)$ that evolves smoothly in time, so $n = 1$ and $\langle \dot{\theta}_p^2 \rangle \sim$ constant for $St_\theta \ll 1$.

For $St_\theta \gg 1$, the integral in (3.7) is dominated by uncorrelated temperature increments, $\delta_t T \sim t^0$, such that $\langle \dot{\theta}_p^2 \rangle \sim St_\theta^{-2}$. The comparison between figure 4(*a*) and figure 5 of Bec *et al.* (2014) highlights the different asymptotic behaviour of $\sigma_{\dot{\theta}_p}^2 \equiv \langle \dot{\theta}_p^2 \rangle$ for $St_\theta \ll 1$, but the same behaviour $\langle \dot{\theta}_p^2 \rangle \sim St_\theta^{-2}$ for $St_\theta \gg 1$. Further, as expected, our DNS data approach these asymptotic regimes for both the cases with and without two-way thermal coupling.

Another difference is that in the results of Bec *et al.* (2014), the tails of the PDFs of $\dot{\theta}_p$ for $St_\theta = 1$ become heavier as St is increased, whereas our results in figure 3 show that while the kurtosis of these PDFs increases from $St = 0.5$ to $St = 1$, it then decreases from $St = 1$ to $St = 3$. In order to examine this further, we performed simulations (without two-way thermal coupling) for $St_\theta = 1$ and $St \leqslant 0.4$. The results are shown in figure 4(*b*), and in this regime we do in fact observe that the tails of the PDFs of $\dot{\theta}_p$ become increasingly wider as St is increased. Taken together with the results in figure 3, this implies that in our simulations, the tails of the PDFs of $\dot{\theta}_p$ become increasingly wider as St is increased until $St \approx 1$, where this behaviour then
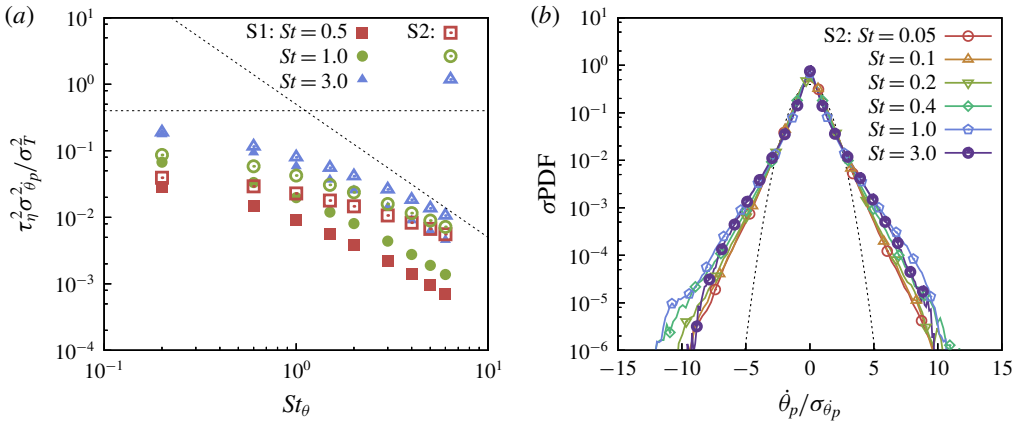
FIGURE 4. (Colour online) (*a*) Variance of the particle temperature rate of change as a function of the thermal Stokes number for different Stokes numbers. The dotted lines represent the expected asymptotic behaviour for $St_\theta \ll 1$ and $St_\theta \gg 1$. (*b*) Normalized PDF of the particle temperature rate of change, $\dot{\theta}_p$ at $St_\theta = 1$ for various Stokes numbers. The dotted line shows a Gaussian PDF for reference. Results obtained neglecting the particle thermal feedback.

saturates, and upon further increase of St the tails start to narrow. This non-monotonic behaviour is due to the particle clustering in the fronts of the temperature field, which is strongest for $St \approx 1$ (see § 5). While the results in Bec *et al.* (2014) over the range $St \leqslant 3.7$ do not show the tails of the PDFs of $\dot{\theta}_p$ becoming narrower, their results clearly show that the widening of the tails saturates (see inset of figure 5 in Bec *et al.* (2014)). It is possible that if they had considered larger St, they would have also begun to observe a narrowing of the tails as St was further increased. Possible reasons why the widening of the tails saturates at a lower value of St in our DNS than it does in theirs include is the effect of Reynolds number ($Re_\lambda = 315$ in their DNS, whereas in our DNS $Re_\lambda = 88$), and differences in the scalar forcing method. This raises the question about Reynolds number dependency. We expect that the strong intermittency of advected passive scalars in high Reynolds number flows may affect the results quantitatively. However, two-way coupled simulations at higher Reynolds numbers are computationally demanding and are left for a future work.

4. Characterization of the temperature fluctuations

This section consists of a short overview of the one-point temperature statistics. Note that due to the large-scale forcing used in the DNS, the one-point statistics of the flow can be affected by the forcing method employed (Dhariwal & Rani 2018). The deterministic forcing may also generate some long standing patterns at large scales. However, the analysed configuration allows us to fix the same average dissipation rate of temperature and velocity fluctuations for all the Stokes numbers considered, which provides considerable advantages for the interpretation of the results.

The statistics of the carrier temperature field, in which the near-particle disturbances are excluded, are presented in this section. As discussed in appendix B, the one-point statistics of the carrier temperature field are very close to the one-point statistics of the actual fluid temperature field in the dilute regime.
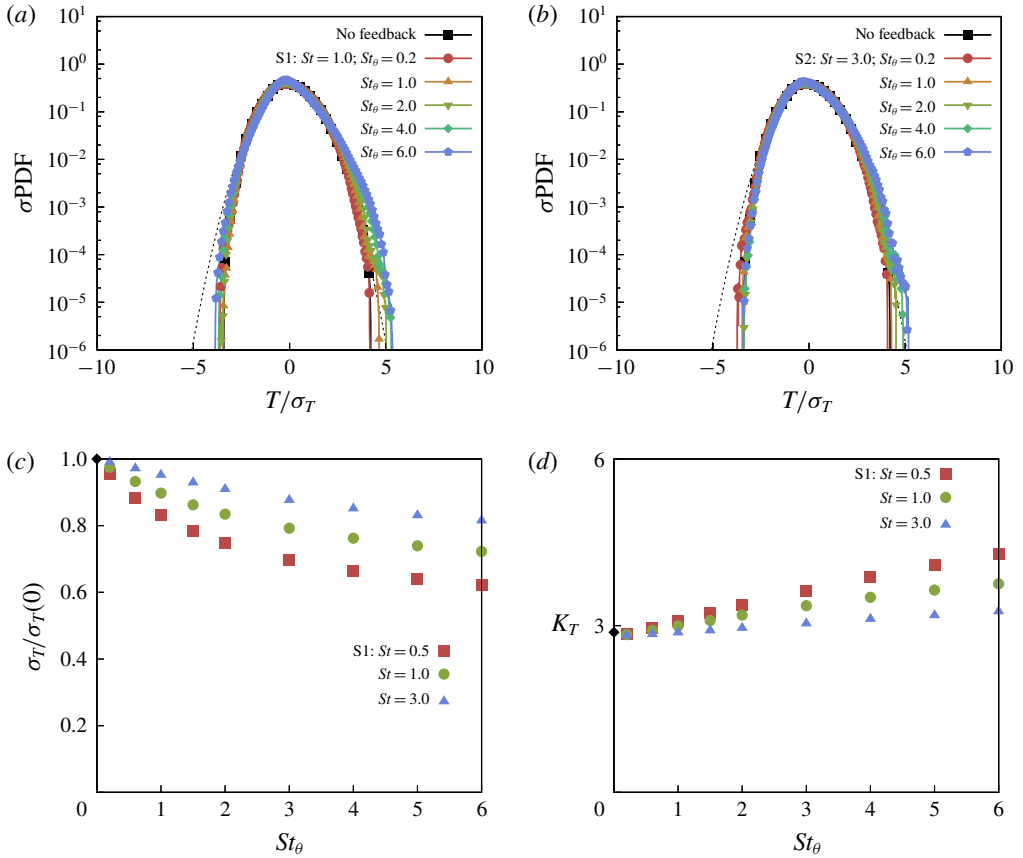
FIGURE 5. (Colour online) PDF of the carrier flow temperature for $St = 1$ (a) and $St = 3$ (b), and for various St_θ. (c) Variance of the carrier flow temperature fluctuations for different St as a function of St_θ. (d) Kurtosis of the carrier flow temperature PDF. These results are from simulations S1 in which the two-way thermal coupling is considered.

4.1. *Fluctuations of the carrier temperature field*

Figure 5(a,b) shows the normalized one-point PDF of the carrier flow temperature for $St = 1$ and $St = 3$, respectively, and for various St_θ. The PDFs are normalized with the standard deviation of the distribution σ_T. The PDFs are almost Gaussian for low St_θ, while the tails become wider as St_θ is increased. However, we are unable to explain the cause of this enhanced non-Gaussianity. The temperature PDFs are also not symmetric, and display a bump in the right tail. This behaviour was also reported by Overholt & Pope (1996) for the case without particles, and it appears to be a low Reynolds number effect that is also dependent on the forcing method employed.

The effect of St on σ_T is striking, whereas we saw earlier in figure 2(c) that χ_f only weakly depends on St. To explain the dependence upon the Stokes number we note that the energy balance (3.2) can be rewritten as

$$\chi = \kappa \left[\langle \|\nabla T\|^2 \rangle + \frac{2}{3} \frac{\phi}{\eta^2} \frac{\rho_p}{\rho_0} \frac{1}{St} \langle (T(\boldsymbol{x}_p, t) - \theta_p)^2 \rangle \right]. \tag{4.1}$$

The factor $\phi\rho_p/(\rho_0\eta^2)$ is constant in our simulations. Therefore, since our DNS data suggest that χ_f is a function of St_θ only (see figure 2c), from (4.1) and (2.3c) we obtain

$$\langle T(\boldsymbol{x}_p, t)^2\rangle - \langle\theta_p^2\rangle \propto St f(St_\theta). \tag{4.2}$$

The kurtosis of the fluid temperature fluctuation is shown in figure 5(d), as a function of St_θ and for various St. For small St_θ, the kurtosis of the fluid temperature fluctuation is close to the value for a Gaussian PDF, namely 3. However, as St_θ is increased, the kurtosis increases. Furthermore, the kurtosis decreases with increasing St for the range considered in our simulations. The explanation of these trends in the kurtosis is unclear.

4.2. *Particle temperature fluctuations*

Figure 6(a,b) shows the normalized one-point PDF of the particle temperature with $St = 1$, for various St_θ, and for simulations S1 and S2. Figure 6(c–d) shows the corresponding results for $St = 3$, and the PDFs are normalized by their standard deviations. When the two-way thermal coupling is accounted for, the tails of the particle temperature distribution tend to become wider as St_θ is increased. On the other hand, when the two-way coupling is neglected, the PDF of the particle temperature is very close to Gaussian, and its shape is not sensitive to either St or St_θ.

The variance of the particle temperature fluctuations monotonically decreases with increasing St_θ, as shown in figure 6(e). The results also show a strong dependence on St, but most interestingly, the dependence on St is the opposite for the cases with and without two-way coupling. To understand this we note that using the formal solution to the equation for $\dot{\theta}_p(t)$ (ignoring initial conditions) we may construct the result

$$\langle\theta_p^2(t)\rangle = \frac{1}{\tau_\theta^2}\int_0^t\int_0^t \langle T(\boldsymbol{x}_p(s), s)T(\boldsymbol{x}_p(s'), s')\rangle \mathrm{e}^{-(2t-s-s')/\tau_\theta}\,\mathrm{d}s\,\mathrm{d}s'. \tag{4.3}$$

If we now substitute into this the exponential approximation

$$\langle T(\boldsymbol{x}_p(s), s)T(\boldsymbol{x}_p(s'), s')\rangle \approx \langle T^2(\boldsymbol{x}_p(t), t)\rangle \exp[-|s - s'|/\tau_T], \tag{4.4}$$

where τ_T is the time scale of $T(\boldsymbol{x}_p(t), t)$, then we obtain

$$\langle\theta_p^2(t)\rangle = \frac{\langle T^2(\boldsymbol{x}_p(t), t)\rangle}{1 + \tau_\theta/\tau_T}. \tag{4.5}$$

This result reveals that the particle temperature variance is influenced by St in two ways. First, $\langle T^2(\boldsymbol{x}_p(t), t)\rangle$ depends upon the spatial clustering of the inertial particles, and this depends essentially upon St. Second, the time scale τ_T is the time scale of the fluid temperature field measured along the inertial particle trajectories, and hence depends upon St. For isotropic turbulence, this time scale is expected to decrease as St is increased, which would lead to $\langle\theta_p^2(t)\rangle$ decreasing as St increases, which is the behaviour observed in figure 6(e). In the presence of two-way coupling, however, $\langle T^2(\boldsymbol{x}, t)\rangle$ increases with increasing St, as shown earlier. In the two-way coupled regime this increase in $\langle T^2(\boldsymbol{x}, t)\rangle$ leads to an increase in $\langle T^2(\boldsymbol{x}_p(t), t)\rangle$ that dominates over the decrease of τ_T with increasing St, and as a result $\langle\theta_p^2(t)\rangle$ increases with increasing St.

The kurtosis of the particle temperature increases with increasing St_θ when the two-way thermal coupling is accounted for, as shown in figure 6(f) (simulations S1, filled symbols). Conversely, the kurtosis of the particle temperature remains constant as St_θ is increased when the two-way thermal coupling is ignored (simulations S2, open symbols).
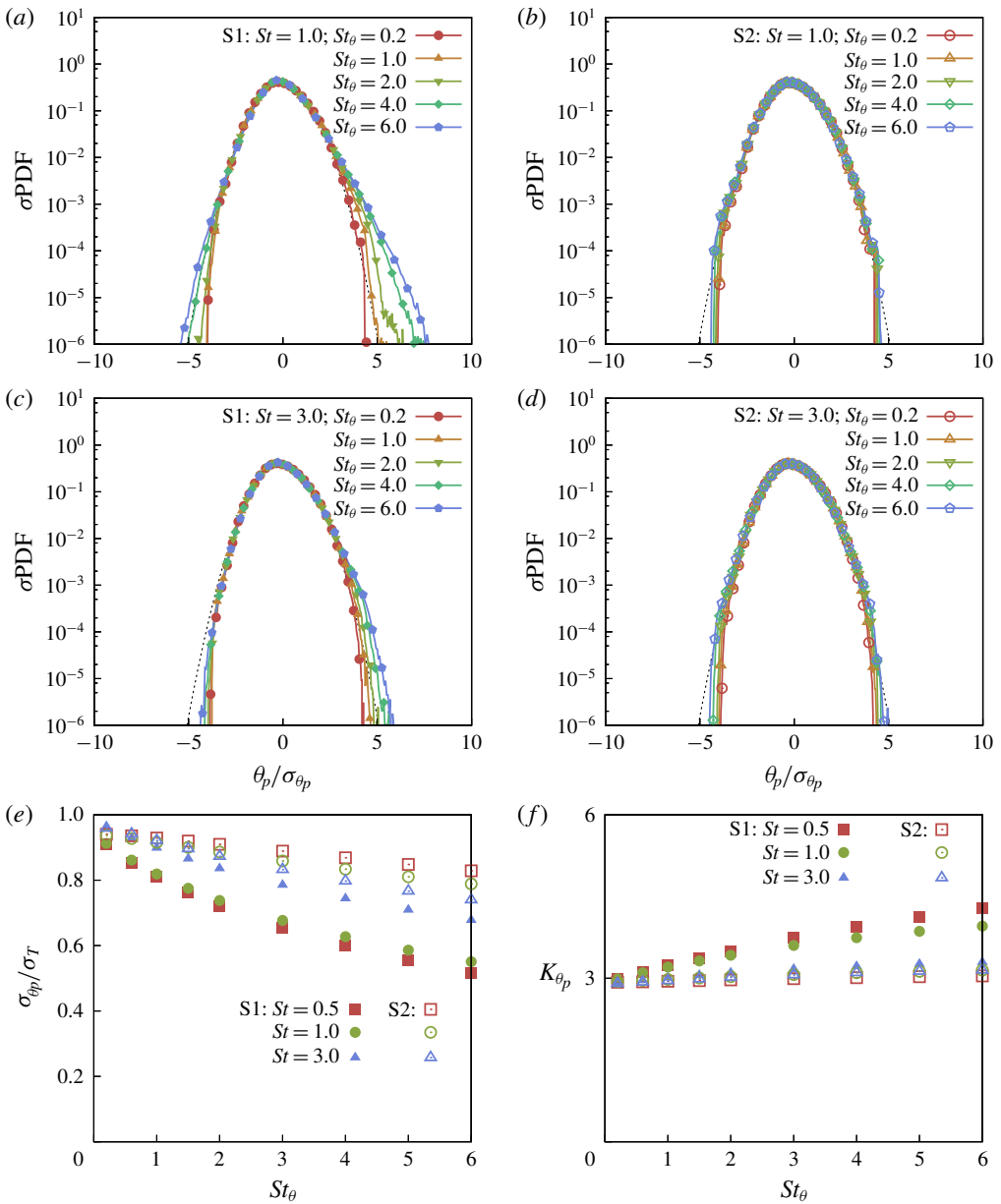
FIGURE 6. (Colour online) PDF of the particle temperature for $St = 1$ (a,b) and $St = 3$ (c,d), for various St_θ. Panels (a–c) are from simulations S1, in which the two-way thermal coupling is considered, while panels (b–d) are from simulations S2, in which the two-way coupling is neglected. (e) Variance of the particle temperature fluctuations for different St numbers as a function of St_θ. (f) Kurtosis of the particle temperature distribution.
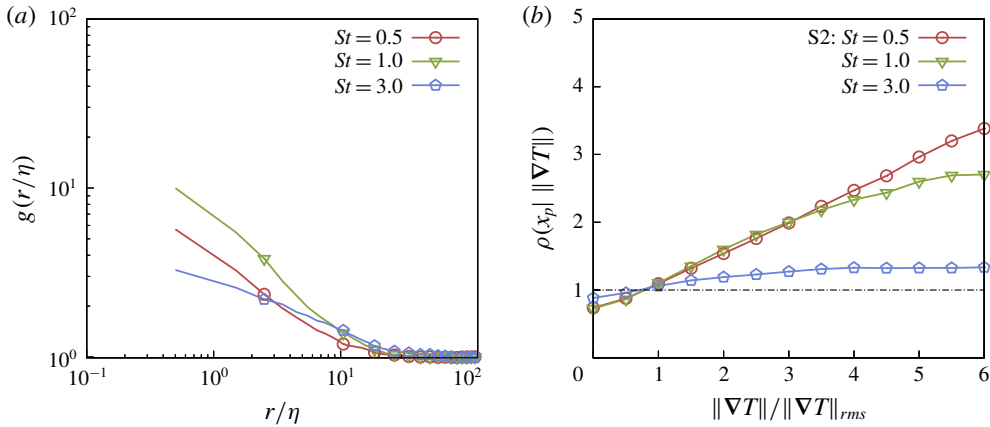
FIGURE 7. (Colour online) (*a*) Radial distribution function (RDF) as a function of the separation r/η for various St. (*b*) Particle number density conditioned on the magnitude of the fluid temperature gradient at the particle position, for various St. These results are from simulations S2, in which the two-way thermal coupling is neglected.

5. Statistics conditioned on the local carrier flow temperature gradients

In this section we consider additional quantities to obtain deeper insight into the one-point particle to fluid heat flux. In particular, we explore the relationship between this heat flux and the local carrier flow temperature gradients.

5.1. *Particle clustering on the temperature fronts*

It is well known that inertial particles in turbulence form clusters (Bec *et al.* 2007), which may be quantified using the radial distribution function (RDF). As shown in figure 7(*a*), the particle number density in our simulations at small separations is a order of magnitude larger than the mean density when $St = O(1)$. Bec *et al.* (2014) showed that inertial particles also exhibit a tendency to preferentially cluster in the fluid temperature fronts where the temperature gradients are large. To demonstrate this, they measured the temperature dissipation rate at the particle positions and showed that this was higher than the Eulerian dissipation rate of the fluid temperature fluctuations. Note that previous works (Gualtieri *et al.* 2013, 2015) have shown that the radial distribution function can be reduced by momentum coupling, which we are neglecting. A future work that includes two-way momentum coupling should consider how this affects the way inertial particles sample high temperature gradients in the flow.

We quantify the tendency for inertial particles to cluster in the fluid temperature fronts by computing the single particle position probability density, conditioned upon the norm of the fluid temperature gradient,

$$\rho(\boldsymbol{x}_p | \|\boldsymbol{\nabla}T\|) = \frac{\rho(\|\boldsymbol{\nabla}T\|(\boldsymbol{x}_p))}{\rho(\|\boldsymbol{\nabla}T\|)}. \tag{5.1}$$

This conditioned probability can also be understood as the ratio between the fraction of inertial particles $n_p(St; \|\boldsymbol{\nabla}T\|)$ located in a region of a given temperature gradient

magnitude $\|\nabla T\|$ and the number of particles $n_p(0; \|\nabla T\|)$ which would be located in the same region for $St \to 0$, that is, when particles follow fluid trajectories,

$$\rho(\boldsymbol{x}_p \mid \|\nabla T\|) = \frac{n_p(St; \|\nabla T\|)}{n_p(0; \|\nabla T\|)}. \tag{5.2}$$

By defining $\|\nabla T\|_{rms}$ as the root mean square (r.m.s.) value of $\|\nabla T\|$, small values of $\|\nabla T\|/\|\nabla T\|_{rms}$ may be interpreted as corresponding to the large scales, and are associated with the Lagrangian coherent structures in which the temperature field is almost constant. Large values of $\|\nabla T\|/\|\nabla T\|_{rms}$ may be interpreted as corresponding to the small scales, and are associated with fronts in the fluid temperature field. The results for $\rho(\boldsymbol{x}_p | \|\nabla T\|)$ are shown in figure 7(*b*), for the simulations without two-way thermal coupling (the results show only a weak dependence on St_θ when the two-way coupling is included). Due to the clustering on the temperature fronts, $\rho(\boldsymbol{x}_p\|\nabla T\|)$ is an increasing function of $\|\nabla T\|$ and it is larger than unity in the region of large temperature gradient. The probability of observing a gradient of a certain magnitude (which is proportional to $n_p(0; \|\nabla T\|)$) decays almost exponentially with increasing $\|\nabla T\|$, as in figure 2(*a*). For values of St at which the maximum particle clustering takes place, $n_p(St; \|\nabla T\|)$ is up to four times larger than $n_p(0; \|\nabla T\|)$ in regions of strong temperature gradients. We expect even higher values at the largest $\|\nabla T\|$, however it is difficult to obtain statistically relevant results in correspondence with such extreme events. These results therefore support the conclusions of Bec *et al.* (2014) that inertial particles preferentially cluster in the fronts of the fluid temperature field where $\|\nabla T\|/\|\nabla T\|_{rms}$ is large.

5.2. *Particle motion across the temperature fronts*

To obtain further insight into the thermal coupling between the particles and fluid we consider the properties of the particle heat flux conditioned on $\|\nabla T\|$. In particular, we consider the following quantity

$$q_n(\|\nabla T\|) \equiv (T(\boldsymbol{x}_p) - \theta_p)^n \boldsymbol{v}_p \cdot \boldsymbol{n}_T(\boldsymbol{x}_p)|_{\|\nabla T\|}, \tag{5.3}$$

where $\boldsymbol{n}_T$ is the normalized, resolved, temperature gradient

$$\boldsymbol{n}_T(\boldsymbol{x}_p) \equiv \frac{\nabla T(\boldsymbol{x}_p)}{\|\nabla T(\boldsymbol{x}_p)\|}. \tag{5.4}$$

The statistics of q_n provide a way to quantify the relationship between the particle heat flux and the local carrier temperature gradients in the fluid. Understanding this relationship is key to understanding how the particles modify the properties of the fluid temperature and temperature gradient fields. It is justified to investigate the interaction between the resolved temperature field, in which the near-particle disturbances are not represented, since, in the dilute regime, particles are statistically far enough that a particle rarely finds itself in the disturbance region of another particle. As discussed in appendix B, the norm of the gradient of the perturbation field induced by the particle is proportional to r_p^{-2} and, therefore, it is usually large.

The efficiency with which the particles cross the fronts in the carrier flow temperature field is quantified by $\langle |q_0| \rangle$, and our results for this quantity in one-way coupled simulations are shown in figure 8(*a*). The curves are normalized with the Kolmogorov velocity scale u_η. At moderate Stokes number, particles tend to
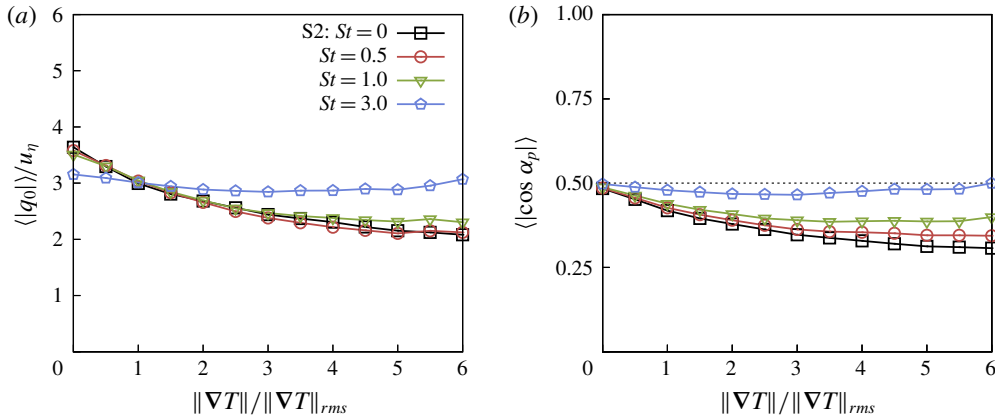
FIGURE 8. (Colour online) (*a*) Results for $\langle |q_0(\|\nabla T\|)| \rangle / u_\eta$, for various St. (*b*) Results for $\langle |\cos \alpha_p| \rangle$ as a function of $\|\nabla T\|$, for various St. These results are from simulations S2, in which the two-way thermal coupling is neglected.

accumulate near the front, therefore they cross the front with a small velocity. On the other hand, particles with large inertia slowly respond to a change of the local velocity/temperature and therefore they are less affected by the local value of the temperature gradient, carrying large temperature increments across the temperature field. Accordingly, the velocity magnitude becomes nearly independent of the local value of the temperature gradient as the particle inertia is increased, as shown in figure 8.

It is also important to consider whether the reduction of $\langle |q_0| \rangle$ as $\|\nabla T\|$ increases is due to the reduction of the norm of the particle velocity or to the lack of alignment between the particle velocity and the fluid temperature gradient at the particle position. Figure 8(*b*) displays the average of the absolute value of the cosine of the angle between the particle velocity and temperature gradient

$$\cos \alpha_p \equiv \frac{\boldsymbol{v}_p}{\|\boldsymbol{v}_p\|} \cdot \frac{\nabla T(\boldsymbol{x}_p)}{\|\nabla T(\boldsymbol{x}_p)\|}, \qquad (5.5)$$

conditioned on $\|\nabla T\|$. The results show that as $\|\nabla T\|$ is increased, the particle motion becomes misaligned with the local carrier flow temperature gradient. This then shows that the reduction of $\langle |q_0| \rangle$ as $\|\nabla T\|$ increases is due to non-trivial statistical geometry in the system. The results also show that as St is increased, the cosine of the angle between the fluid temperature gradient and the particle velocity becomes almost independent of $\|\nabla T\|$, and $\langle |\cos \alpha_p| \rangle \approx 1/2$, the value corresponding to $\cos \alpha_p$ being a uniform random variable. This shows that as St is increased, the correlation between the direction of the particle velocity and the local carrier fluid velocity gradient vanishes.

5.3. *Heat flux due to the particle motion across the fronts*

We now turn to consider the quantity $\langle q_1 \rangle$. When the particle moves from a cold to a warm region of the fluid, the component of the particle velocity along the temperature gradient is positive, $\boldsymbol{v}_p \cdot \boldsymbol{n}_T(\boldsymbol{x}_p) > 0$. If the particle is also cooler than the local fluid so that $T(\boldsymbol{x}_p) - \theta_p > 0$, then as it moves into the region where the fluid is warmer,

$q_1 > 0$ meaning that the particle will absorb heat from the fluid, and will therefore tend to reduce the local fluid temperature gradient. When the particle moves from a warm to a cold region of the flow, if $T(\boldsymbol{x}_p) - \theta_p < 0$ then q_1 is also positive, so that again the particle will act to reduce the local temperature gradient in the fluid. Therefore, $q_1 > 0$ indicates that the action of the inertial particles is to smooth out the fluid temperature field, reducing the magnitude of its temperature gradients, and $q_1 < 0$ implies the particles enhance the temperature gradients.

The results for $\langle q_1 \rangle$ are shown in figure 9 for various St and St_θ, including (simulations S1) and neglecting (simulations S2) the two-way thermal coupling. On average we observe $\langle q_1 \rangle \geqslant 0$, such that the particles tend to make the fluid temperature field more uniform. The results show that $\langle q_1 \rangle$ tends to zero as $\|\boldsymbol{\nabla} T\| \to 0$. This indicates that the particles spend enough time in the Lagrangian coherent structures to adjust to the temperature of the fluid. However, $\langle q_1 \rangle$ increases significantly as $\|\boldsymbol{\nabla} T\|$ increases, suggesting that inertial particles can carry large temperature differences across the fronts. In the limit $St_\theta \to 0$, $\langle q_1 \rangle \to 0$ reflecting the thermal equilibrium between the particles and the fluid. As St_θ is increased, the heat flux becomes finite, however, if St_θ is too large, the particle temperature decorrelates from the fluid temperature and the heat exchange is not effective. Hence, $\langle q_1 \rangle$ can saturate with increasing St_θ. The results show that $\langle q_1 \rangle$ increases with increasing St, associated with the decoupling of $\boldsymbol{v}_p$ and $\boldsymbol{n}_T(\boldsymbol{x}_p)$ discussed earlier. Finally, the results also show that two-way thermal coupling reduces $\langle q_1 \rangle$. This is simply a reflection of the fact that since the particles tend to smooth out the fluid temperature gradients, the disequilibrium between the particle and local fluid temperature is reduced, which in turn reduces the heat flux due to the particles.

6. Temperature structure functions

We now turn to consider two-point quantities in order to understand how the two-way thermal coupling affects the system at the small scales.

6.1. *Structure functions of the carrier temperature field*

The nth-order structure function of the resolved fluid temperature field is defined as

$$S_T^n(r) \equiv \langle |\Delta T(r, t)|^n \rangle, \tag{6.1}$$

where $\Delta T(r, t)$ it the difference in the carrier temperature field at two points separated by the distance r (the 'temperature increment'). The results for S_T^2, with different St and St_θ are shown in figure 10. The structure functions of the actual temperature field differ from the structure functions of the carrier temperature field, due to the near-particle temperature disturbances. As discussed in appendix B, the impact of the local near-particle perturbation is marked at small separation and the carrier flow temperature field can be understood as the actual temperature field filtered at the grid resolution scale. In order to emphasize this fact, the carrier flow temperature structure functions are reported only down to the Kolmogorov scale, which is comparable to the grid spacing.

The results show that S_T^2 decreases monotonically with increasing St_θ at all scales when the two-way thermal coupling is taken to account. In the dissipation range, S_T^2 is directly connected to the dissipation rate, and is suppressed in the same way for the three different St considered. Conversely, the suppression of the large-scale fluctuations is stronger as St is reduced, at least for the range of St considered here.
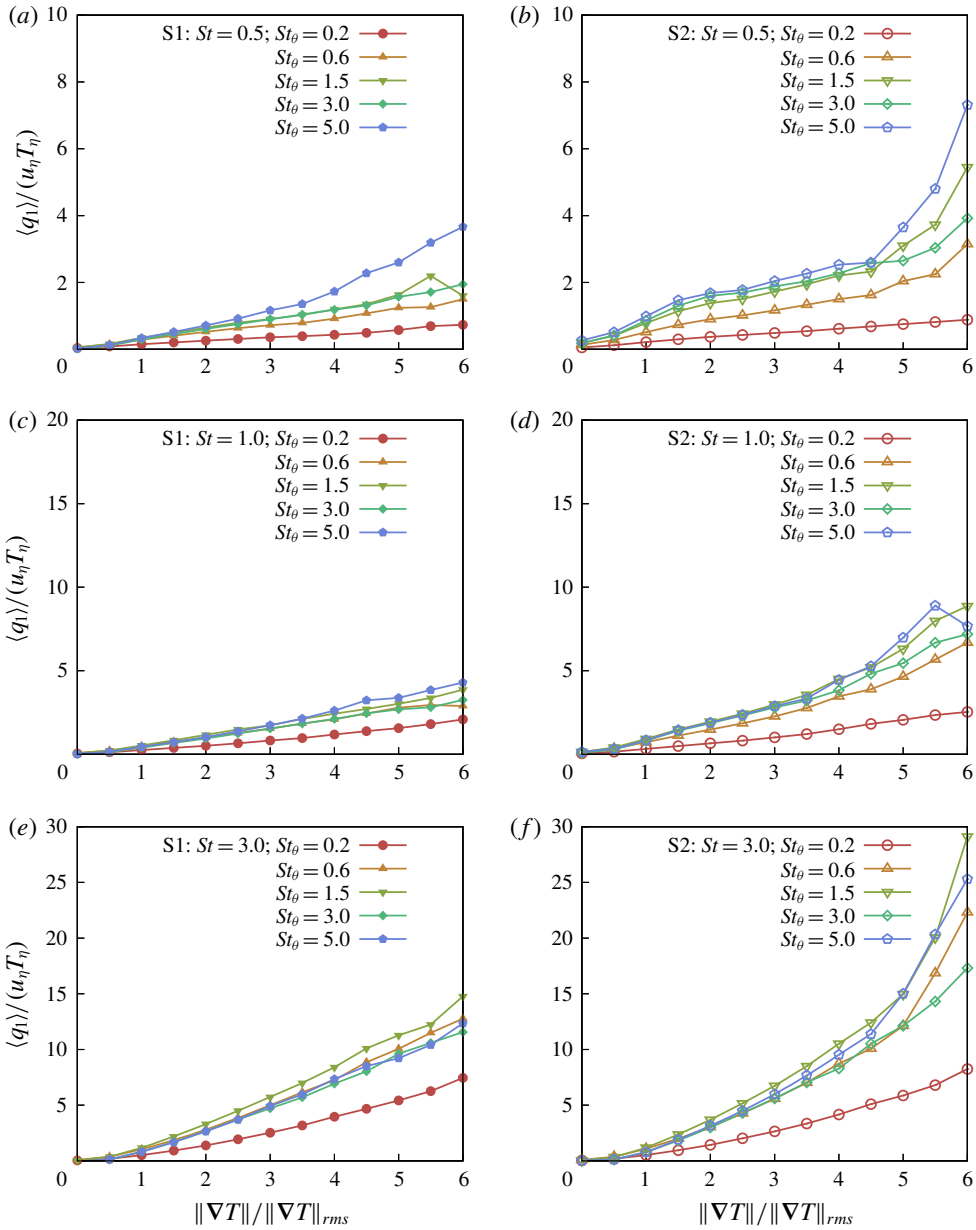
FIGURE 9. (Colour online) Results for $\langle q_1(\|\boldsymbol{\nabla}T\|)\rangle/(u_\eta T_\eta)$ for $St = 0.5$ (a,b), $St = 1$ (c,d) and $St = 3$ (e,f) and for various St_θ. Panels (a,c,e) are from simulations S1, in which the two-way thermal coupling is considered, while panels (b,d,f) are from simulations S2, in which the two-way coupling is neglected.

The scaling exponents of the structure functions of the carrier temperature field
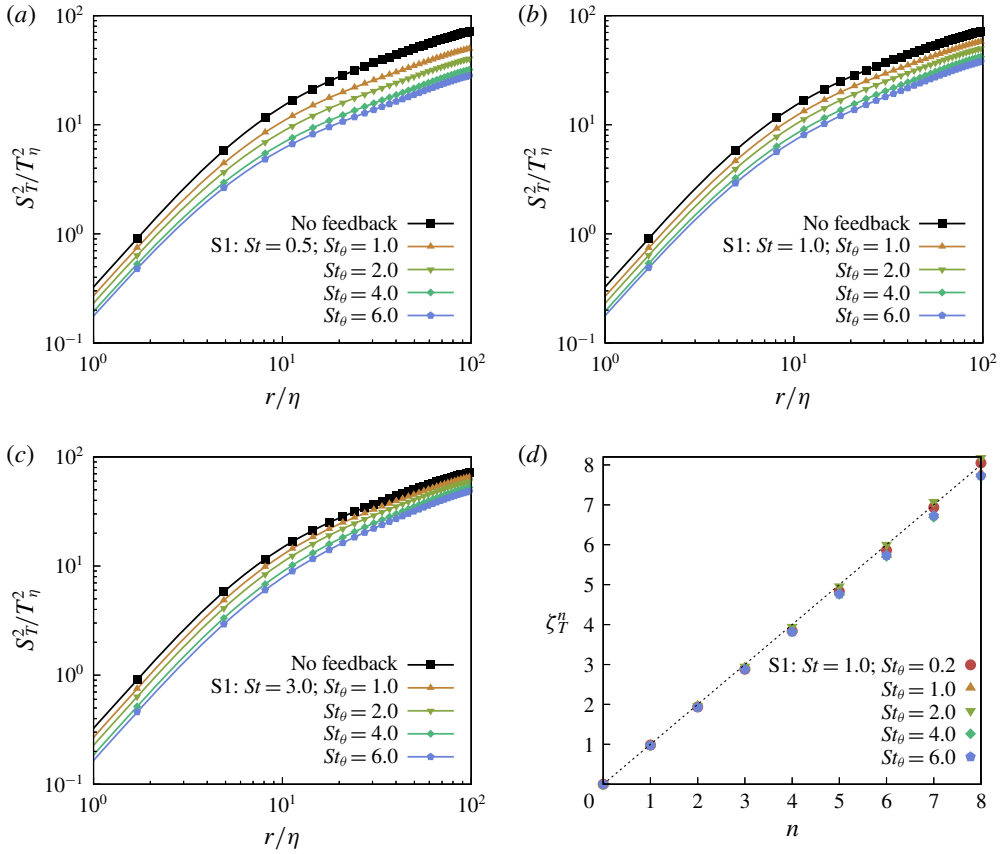
$$\zeta_T^n \equiv \frac{\mathrm{d}\log \mathrm{S}_T^n(r)}{\mathrm{d}\log r} \tag{6.2}$$

FIGURE 10. (Colour online) Results for S_T^2 for different St_θ, for $St = 0.5$ (*a*), $St = 1$ (*b*) and $St = 3$ (*c*). (*d*) Scaling exponents of the fluid temperature structure functions at small separation, $r \leqslant 2\eta$, at $St = 1$. The data are from simulations S1 in which the two-way thermal coupling is considered.

are shown in figure 10(*d*) for $r \leqslant 2\eta$. The results show that the resolved fluid temperature field remains smooth (to within numerical uncertainty) even when inertial particles are suspended in the flow.

6.2. *Particle temperature structure functions*

The *n*th-order structure function of the particle temperature $\theta_p(t)$ is defined as

$$S_\theta^n(r) \equiv \langle |\Delta\theta_p|^n \rangle_r, \tag{6.3}$$

where $\Delta\theta_p(t)$ is the difference in the temperature of the two particles, and the brackets denote an ensemble average, conditioned on the two particles having separation r. The results for S_θ^2 for different St and St_θ, with and without two-way thermal coupling, are shown in figure 11.

The results show that S_θ^2 depends on St_θ in much the same way as the inertial particle relative velocity structure functions depend on St (Ireland *et al.* 2016*a*). This is not surprising since the equation governing $\dot\theta_p$ is structurally identical to the
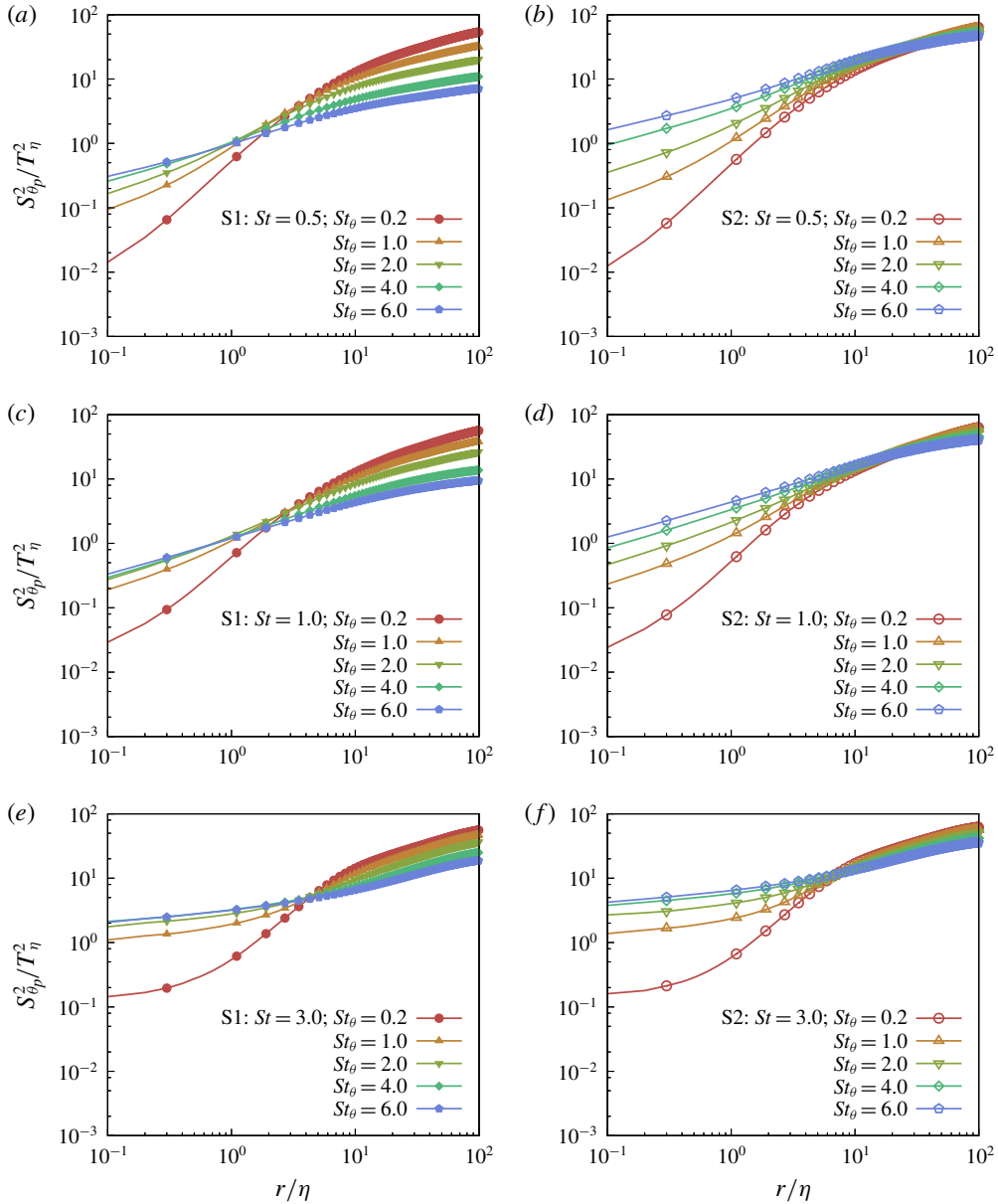
FIGURE 11. (Colour online) Results for S_θ^2 for different St_θ, for $St = 0.5$ (*a,b*), $St = 1$ (*c,d*) and $St = 3$ (*e,f*). Panels (*a,c,e*) are from simulations S1, in which the two-way thermal coupling is considered, while panels (*b,d,f*) are from simulations S2, in which the two-way coupling is neglected.

equation governing the particle acceleration. However, important differences are that $\dot{\theta}_p$ depends on both St and St_θ, and also that the fluid temperature field is structurally different from the fluid velocity field, with the temperature field exhibiting the well-known ramp–cliff structure.

To obtain further insight into the behaviour of S_θ^2 and S_θ^n in general, we note that the formal solution for $\Delta\theta_p(t)$ is given by (ignoring initial conditions)

$$\Delta\theta_p(t) = \frac{1}{\tau_\theta} \int_0^t \Delta T(\boldsymbol{x}_p(s), \boldsymbol{r}_p(s), s) \exp\left(-\frac{t-s}{\tau_\theta}\right) \, \mathrm{d}s, \qquad (6.4)$$

where $\Delta T(\boldsymbol{x}_p(s), \boldsymbol{r}_p(s), s)$ is the difference in the fluid temperature at the two particle positions $\boldsymbol{x}_p(s)$ and $\boldsymbol{x}_p(s) + \boldsymbol{r}_p(s)$. Equation (6.4) shows that $\Delta\theta_p(t)$ depends upon ΔT along the path history of the particles, and $\Delta\theta_p(t)$ is therefore a non-local quantity. The role of the path history increases as St_θ is increased since the exponential kernel in the convolution integral decays more slowly as τ_θ is increased. Since the statistics of ΔT increase with increasing separation, particle pairs at small separations are able to be influenced by larger values of ΔT along their path history, such that $\Delta\theta_p(t)$ can significantly exceed the local fluid temperature increment $\Delta T(\boldsymbol{x}_p(t), \boldsymbol{r}_p(t), t)$. This then causes S_θ^2 to increase with increasing St_θ, as shown in figure 11. This effect is directly analogous to the phenomena of caustics that occur in the relative velocity distributions of inertial particles at the small scales of turbulence (Wilkinson & Mehlig 2005), and which occur because the inertial particle relative velocities depend non-locally on the fluid velocity increments experienced along their trajectory history (Bragg & Collins 2014b). In analogy, we may therefore refer to the effect as 'thermal caustics', and they may be of particular importance for particle-laden turbulent flows where particles in close proximity thermally interact.

The results in figure 11 also reveal a strong effect of St, and one way that St affects these results is through the spatial clustering and preferential sampling of the fluid temperature field by the inertial particles. There is, however, another mechanism through which St can affect S_θ^2. In particular, since, due to caustics, the relative velocity of the particles increases with increasing St at the small scales, then the values of $\Delta T(\boldsymbol{x}_p(s), \boldsymbol{r}_p(s), s)$ that may contribute to $\Delta\theta_p(t)$ become larger. This follows since if their relative velocities are larger, then over the time span $t - s \leqslant O(\tau_\eta)$ the particle pair can come from even larger scales where (statistically) $\Delta T(\boldsymbol{x}_p(s), \boldsymbol{r}_p(s), s)$ is bigger. This effect would cause S_θ^2 to increase with St for a given St_θ, further enhancing the thermal caustics, which is exactly what is observed in figure 11. The results also show that the thermal caustics are stronger for $St_\theta \geqslant O(1)$ when the two-way thermal coupling is ignored. This is mainly due to the reduction in the fluid temperature gradients due to the two-way thermal coupling described earlier, noting that in the limit of vanishing fluid temperature gradients, the thermal caustics necessarily disappear.

At larger scales where the statistics of ΔT vary more weakly with r, the non-local effect weakens, the thermal caustics disappear, and a filtering mechanism takes over which causes S_θ^2 to decrease with increasing St_θ. This filtering effect is directly analogous to that dominating the large-scale velocities of inertial particles in isotropic turbulence, and is associated with the sluggish response of the particles to the large-scale flow fluctuations due to their inertia (Ireland *et al.* 2016a).

The particle temperature structure functions S_θ^n behave as power laws at small separation, $\log S_\theta^n(r) \approx \zeta_\theta^n \log r + a^n$, and the associated scaling exponents ζ_θ^n are shown in figure 12. The exponents are obtained by fitting the logarithm of the structure function in the dissipation range according to ordinary least squares. To reduce statistical noise, we estimate ζ_θ^n by fitting the data for S_θ^n over the range $0.2\eta \leqslant r \leqslant 2\eta$. Over this range, S_θ^n do not strictly behave as power laws, and
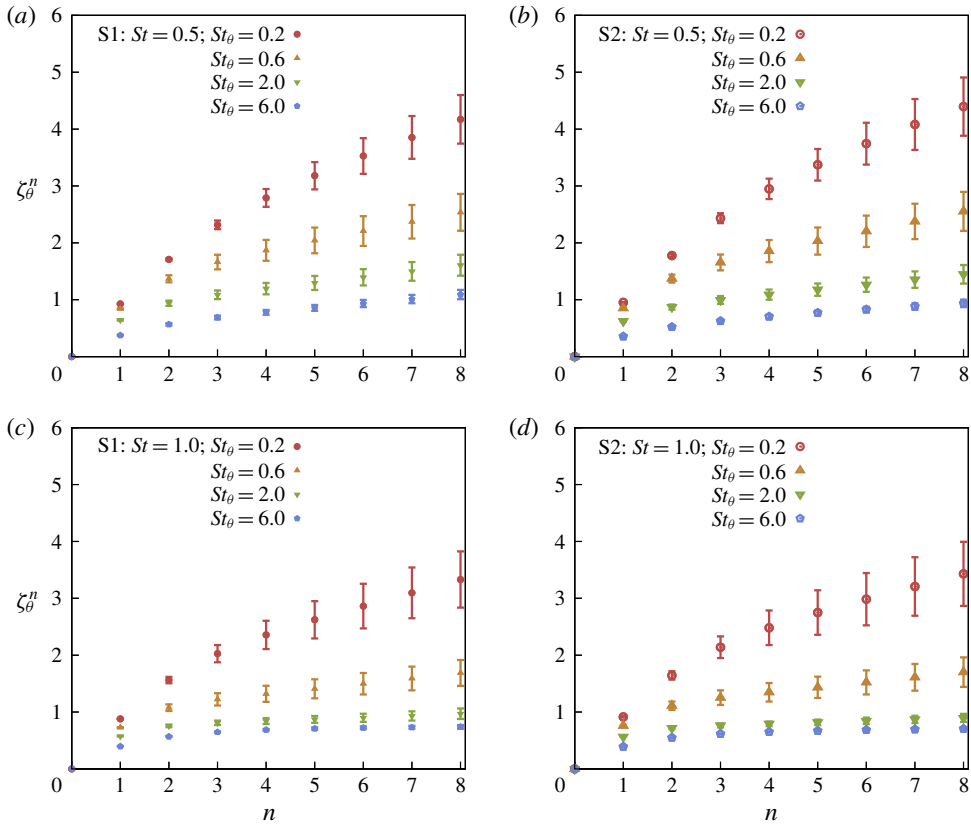
FIGURE 12. (Colour online) Scaling exponent of the structure functions of the particle temperature at small separation, $0.2\eta \leqslant r \leqslant 2\eta$, for various thermal Stokes numbers St_θ, at fixed Stokes number $St = 0.5$ (a,b) and $St = 1$ (c,d). Panels (a,c) are from simulations S1, in which the two-way thermal coupling is considered, while panels (b,d) are from simulations S2, in which the two-way coupling is neglected.

hence the exponents measured are understood as average exponents. The error bars indicate the largest deviations from the mean exponent observed in the considered range. The results in figure 12 reveal that particle temperature increments exhibit a strong multifractal behaviour. This multifractality is due to the non-local thermal dynamics of the particles and the formation of thermal caustics, described earlier. In particular, there exists a finite probability to find inertial particle pairs that are very close but have large temperature differences because they experienced very different fluid temperatures along their trajectory histories. As with the thermal caustics, the multifractality is enhanced as St is increased. Most interestingly, the results for ζ_θ^n are only weakly affected by the two-way thermal coupling, despite the fact that we observed a significant effect of the coupling on S_θ^2. This suggests that the two-way coupling affects the strength of the thermal caustics, but only weakly affects the scaling of the structure functions in the dissipation range.
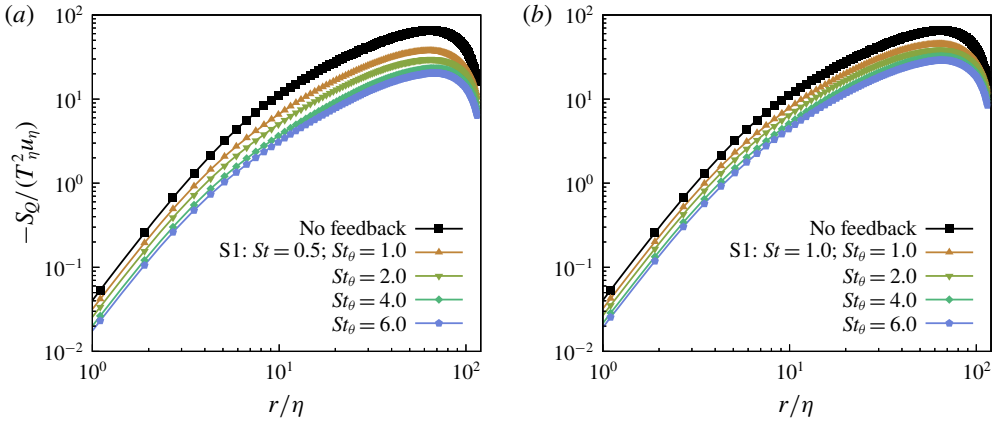
FIGURE 13. (Colour online) Second-order mixed structure functions of the carrier flow temperature field, for different thermal Stokes numbers of the suspended particles, at $St = 0.5$ (*a*) and $St = 1$ (*b*). The data refer to the set of simulations S1, with thermal particle back reaction included.

6.3. *Mixed structure functions*

We turn to considering the behaviour of the flux of the temperature increments across the scales of the flow, which is associated with the mixed structure functions

$$S_Q(r) \equiv \langle (\Delta T(r, t))^2 \Delta u_{\parallel}(r, t) \rangle, \tag{6.5}$$

where $\Delta u_{\parallel}$ is the longitudinal relative velocity difference. The results for S_Q, for different St and St_{θ} are shown in figure 13. Just as we observed for the fluid temperature structure functions, $-S_Q$ decreases monotonically with increasing St_{θ}, as was also observed for the fluid temperature dissipation rate χ_f. The mixed structure functions of the carrier temperature field are reported to separation down to the Kolmogorov scale, that is the scale at which the carrier temperature field is resolved, as discussed in appendix B.

To consider the flux of the particle temperature increments, we begin by considering the exact equation that can be constructed for S_{θ}^n using PDF transport equations. In particular, if we introduce the PDF $\mathcal{P}(r, \Delta\theta, t) \equiv \langle \delta(r_p(t) - r)\delta(\Delta\theta_p(t) - \Delta\theta) \rangle$ and the associated marginal PDF $\varrho(r, t) \equiv \int \mathcal{P} \, d\Delta\theta$, where r and $\Delta\theta$ are time-independent phase-space coordinates, then we may derive for a statistically stationary system the result (see Bragg & Collins (2014*a*), Bragg *et al.* (2015*b*) for details on how to derive such results)

$$\langle [\Delta\theta_p(t)]^2 \rangle_r = \langle \Delta T(x_p(t), r_p(t), t)\Delta\theta_p(t) \rangle_r - \frac{\tau_{\theta}}{2\varrho} \frac{\partial}{\partial r} \cdot \varrho \langle [\Delta\theta_p(t)]^2 w_p(t) \rangle_r, \tag{6.6}$$

where $w_p(t) \equiv \partial_t r_p(t)$. The first term on the right-hand side is the local contribution that remains when there exist no fluxes across the scales, and this term determines the behaviour of $\langle [\Delta\theta_p(t)]^2 \rangle_r$ at the large scales of homogeneous turbulence where the statistics are independent of r. The second term on the right-hand side is the non-local contribution that arises for $St_{\theta} > 0$, and it is this term that is responsible for the thermal caustics discussed earlier. It depends on the spatial clustering of the particles
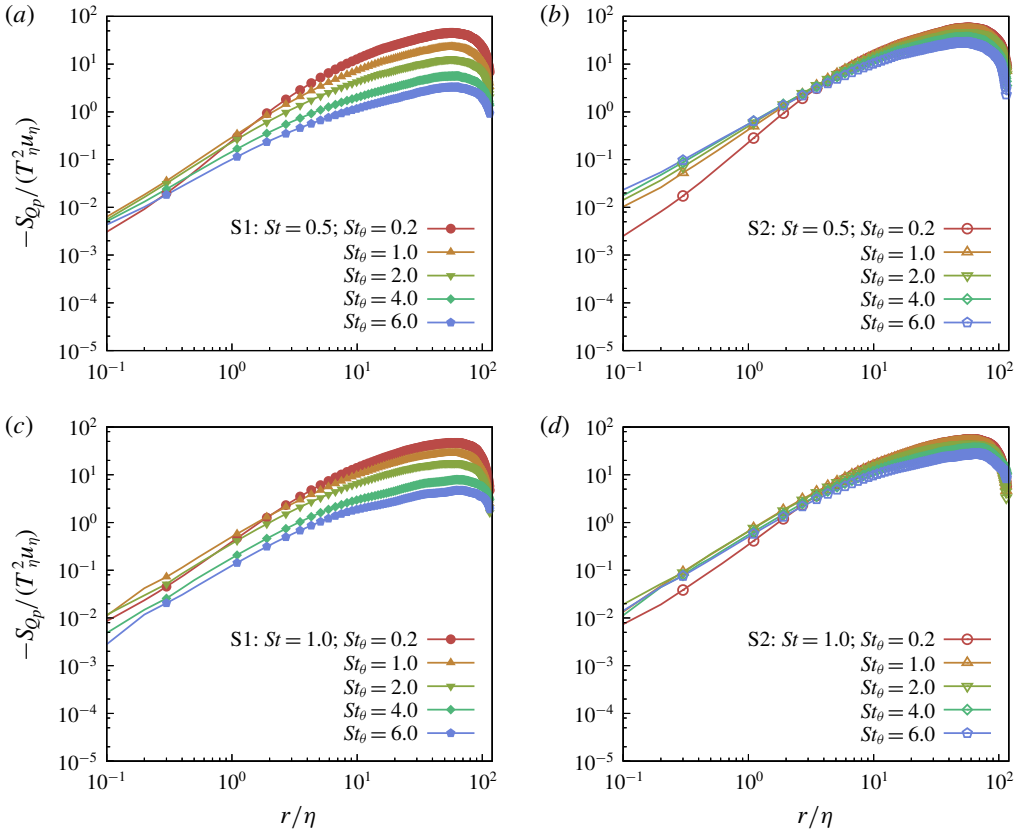
FIGURE 14. (Colour online) Second-order mixed structure functions of the particle temperature, for different thermal Stokes numbers, at $St = 0.5$ (*a,b*) and $St = 1$ (*c,d*). Panels (*a,c*) refer to the set of simulations S1, in which the thermal particle back reaction is included. Panels (*b,d*) refer to the set of simulations S2, in which the thermal particle back reaction is neglected.

through ϱ (which is proportional to the RDF), and the flux $\langle [\Delta\theta_p(t)]^2 \boldsymbol{w}_p(t) \rangle_r$ which, for an isotropic system, is determined by the longitudinal component

$$S_{Q_p}(r) \equiv \frac{\boldsymbol{r}}{r} \cdot \langle [\Delta\theta_p(t)]^2 \boldsymbol{w}_p(t) \rangle_r. \tag{6.7}$$

The results for S_{Q_p} from our simulations are shown in figure 14, and they show that without two-way coupling, $-S_{Q_p}$ monotonically increases with increasing St_θ at the smallest scales. However, with two-way coupling, $-S_{Q_p}$ is maximum for intermediate values of St_θ, and this occurs because as shown earlier, as St_θ is increased, the fluid temperature fluctuations are suppressed across the scales.

7. Distribution of the temperature fluxes

We finally look at the distribution of temperature flux across the scales, in the dissipation range. We consider the PDFs of the carrier flow temperature flux $Q = (\Delta T(r, t))^2 \Delta u_\parallel (r, t)$ and particle temperature flux $Q = [\Delta\theta_p(t)]^2 w_\parallel(t)$, where $w_\parallel(t)$ is the parallel component of the particle-pair relative velocity.
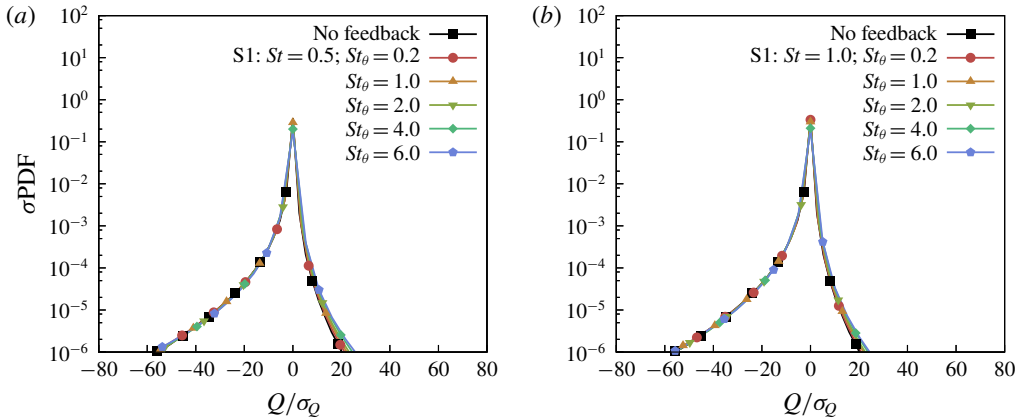
FIGURE 15. (Colour online) PDF in normal form of the flux of carrier flow temperature increments at small separations, $r \leqslant 2\eta$, at $St = 0.5$ (a) and $St = 1$ (b). The data refer to the set of simulations S1, with thermal feedback included.

The PDF of the carrier flow temperature flux, which does not include the contribution of the near-particle field changes, is plotted in normal form for $r \leqslant 2\eta$ in figure 15. These normalized PDFs collapse onto each other for all St and St_θ values considered. Thus, the distribution of the resolved temperature increments flux simply scales with its variance in the dissipation range, and the variance of the flux is modulated by the particles but the shape of the distribution is not affected by the particle dynamics. The PDFs are strongly negatively skewed and have a negative mean value, associated with the mean flux of thermal fluctuations from large to small scales in the flow.

The PDF of the particle temperature flux is plotted in normal form for $r \leqslant 2\eta$ in figure 16. The PDF of the particle temperature flux across the scales is not self-similar with respect to its variance. Furthermore, the PDF becomes more symmetric as St_θ is increased. This is associated with the increasingly non-local thermal dynamics of the particles, which allows the particle pairs to traverse many scales of the flow with minimal changes in their temperature difference.

8. Conclusions

Using direct numerical simulations, we have investigated the interaction between the scalar temperature field and the temperature of inertial particles suspended in the fluid, with one- and two-way thermal coupling, in statistically stationary, isotropic turbulence.

We found that the shape of the PDF of the carrier flow temperature gradients is not affected by the presence of the particles when two-way thermal coupling is considered, and scales with its variance. On the other hand, the variance of the fluid temperature gradients decreases with increasing St_θ, while St plays a negligible role. The PDF of the rate of change of the particle temperature, whose variance is associated with the thermal dissipation due to the particles, does not scale in a self-similar way with respect to its variance, and its kurtosis decreases with increasing St_θ. The particle temperature PDFs and their moments exhibit qualitatively different dependencies on St for the case with and without two-way thermal coupling.
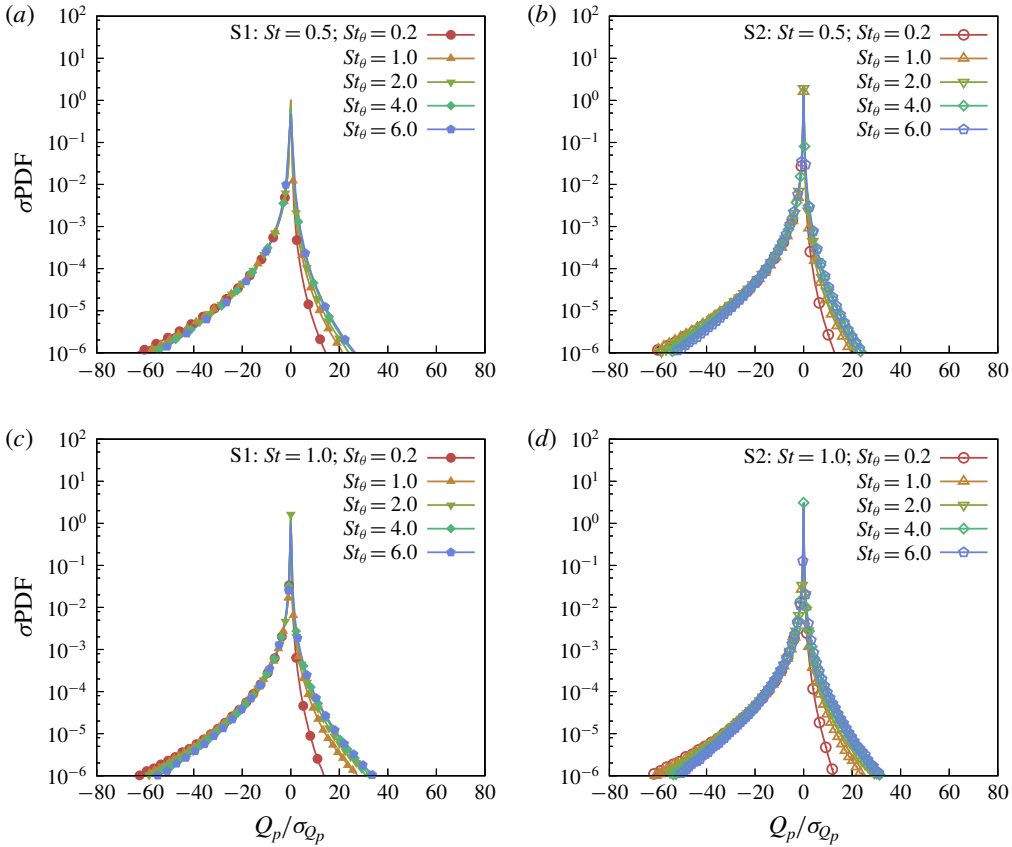
FIGURE 16. (Colour online) PDF in normal form of the flux of particle temperature increments at small separations, $r \leqslant 2\eta$, at $St = 0.5$ (a,b), $St = 1$ (c,d). Panels (a,c) refer to the set of simulations S1, in which the thermal particle back reaction is included. Panels $(b–d)$ refer to the set of simulations S2, in which the thermal particle back reaction is neglected.

To obtain further insight into the fluid–particle thermal coupling, we computed the number density of particles conditioned on the magnitude of the local fluid temperature gradient. In agreement with Bec *et al.* (2014), we observed that the particles cluster in the fronts of the temperature field. We also computed quantities related to moments of the particle heat flux conditioned on the magnitude of the local carrier flow temperature gradient. These results showed how the particles tend to decrease the fluid temperature gradients, and that this is associated with the statistical alignments of the particle velocity and the local carrier flow temperature gradient field.

The two-point temperature statistics were then examined to understand the properties of the temperature fluctuations across the scales of the flow. By computing the structure functions, we observed that the fluctuations of the carrier flow temperature increments are monotonically suppressed as St_θ increases in the two-way coupled regime. The structure functions of the particle temperatures revealed the dominance of thermal caustics at the small scales, wherein the particle temperature differences at small separations rapidly increase as St_θ and St are increased. This

allows particles to come into contact with very large temperature differences, which has a number of important practical implications. The scaling exponents of the inertial particle temperature structure functions in the dissipation range revealed strongly multifractal behaviour.

Finally, the flux of carrier flow temperature increments across the scales was found to decrease monotonically with increasing St_θ. The PDFs of this flux are strongly negatively skewed and have a negative mean value, indicating that the flux is predominately from the large to the smallest scales of the flow. In the two-way coupled regime, the presence of the inertial particles does not change the shape of the PDF. The PDF of the flux of particle temperature increments in the dissipation range becomes more and more symmetric as St_θ is increased, associated with the increasingly non-local thermal dynamics of the particles.

The results presented have revealed a number of non-trivial effects and behaviours of the particle temperature statistics. In a future work it will be important to consider the role of gravitation settling and coupling with water vapour fields, both of which are important for the cloud droplet problem. Moreover, it will be interesting to include the two-way momentum coupling and to consider the non-dilute regime.

Appendix A. Influence of momentum coupling and elastic collisions

In this appendix we quantify the effects of two-way momentum coupling and elastic collisions, which have been neglected in our simulations.

A.1. *Momentum coupling*

Concerning the momentum coupling, we have carried out a few numerical simulations in which both momentum and temperature coupling are taken to account. The results show that the small-scale statistics are only weakly affected by the momentum coupling. The thermal dissipation rate at different Stokes and thermal Stokes numbers, with and without momentum coupling, is shown in figure 17(*a*), which shows that the impact of two-way momentum coupling is quite small. As expected, the effect of the momentum coupling is more evident for large Stokes numbers ($St = 3$), but even then the effect is quite small. A small reduction of the thermal dissipation due to the particles is observed since the large heat flux towards the particles is mainly a consequence of the concentration of particles in the regions of large temperature gradients, yet we expect a smoothing of the velocity field by momentum two-way coupling, which mitigates the particle preferential concentration in the vicinity of the temperature fronts. The second-order structure functions of the carrier temperature field at $St = 3$ are shown in figure 17(*b*). Small quantitative modifications of the fluid temperature occur due to the momentum coupling, especially at large separation,

but, more importantly, the overall picture is not modified. Moreover, it should be noted that the actual Stokes number is modified by the two-way momentum coupling, since the fluid dissipation rate is no longer equal to the energy injection rate in (2.2), resulting in a longer Kolmogorov time scale. Data in figure 17 are presented using the nominal Kolmogorov time scale obtained by using overall dissipation rate, that is, the same scale of simulations without particle momentum feedback. These results justify our neglect of two-way momentum coupling in the current study as a first approximation.

A.2. *Elastic collisions*

According to the criterion by Elghobashi (1994), the upper limit of the volume fraction for the validity of the two-way coupling is $\phi = 10^{-3}$. Above this threshold particle–particle interactions become frequent. Since in our work $\phi = 4 \times 10^{-4}$ and the Stokes number can be of order one, we have re-run some of the simulations taking into account particle–particle interactions assuming elastic collisions. Apart of collisions, any direct small-scale hydrodynamic interaction (Onishi, Takahashi & Vassilicos 2013) is not taken into account.

The particle path is reconstructed at first order between time t_n and $t_{n+1} = t_n + \Delta t$, where Δt is the time step employed in the simulations. This yields the following second-order equation for the relative distance between the pth and qth particle,

$$\|(1 - \tilde{t})(\boldsymbol{x}_p(t_n) - \boldsymbol{x}_q(t_n)) + \tilde{t}(\boldsymbol{x}_p(t_{n+1}) - \boldsymbol{x}_q(t_{n+1}))\| = 2r_p, \tag{A 1}$$

where $\tilde{t} = (t - t_n)/\Delta t$. If a real solution $\tilde{t} \in [0, 1)$ exists, a collision is detected and the colliding particles p and q are evolved according to the equations for elastic collisions between rigid spheres. No heat exchange occurs during the instantaneous collision. Numerically, the direct search for collisions would be impractical, since it would require $O(N_P^2)$ operations. In our simulations, the search for collisions is performed by grouping the particles inside small boxes and searching inside each box (Onishi *et al.* 2013). The spurious effect of the box boundaries is removed translating the boxes and repeating the search.

The results show that, in the parameter range we are considering, the collisions only mildly affect the heat exchange between the carrier fluid and the particles. As shown in figure 17(*a*), the change in the thermal dissipation rate due to the carrier temperature gradient is very moderate when elastic collisions are taken to account. The effect of elastic collisions on the carrier flow temperature structure functions is negligible, as in figure 17(*b*). The effect of elastic collisions on the scaling exponents of the particle temperature structure functions at small separation is shown figure 17(*c*). The impact of elastic collisions on those statistics at $St = 1$ is more noticeable but still moderate. The temperature difference between colliding particles is shown in figure 17(*c*), for $St = 0.5$, 1 and 3 and corresponding $St_\theta = 0.6$, 1 and 3. Due to the intermittency of the carrier flow temperature gradient and to the path-history effect, the relative temperature between colliding particles can be large with respect to the small-scale temperature increment T_η. However, such large temperatures rarely occur and the majority of the temperature increments are concentrated in $|\Delta T| < T_\eta$, a behaviour similar to that of relative velocity distribution between colliding particles (Voßkuhle *et al.* 2014). The relative temperature between colliding particles increases with the particle inertia, as expected.
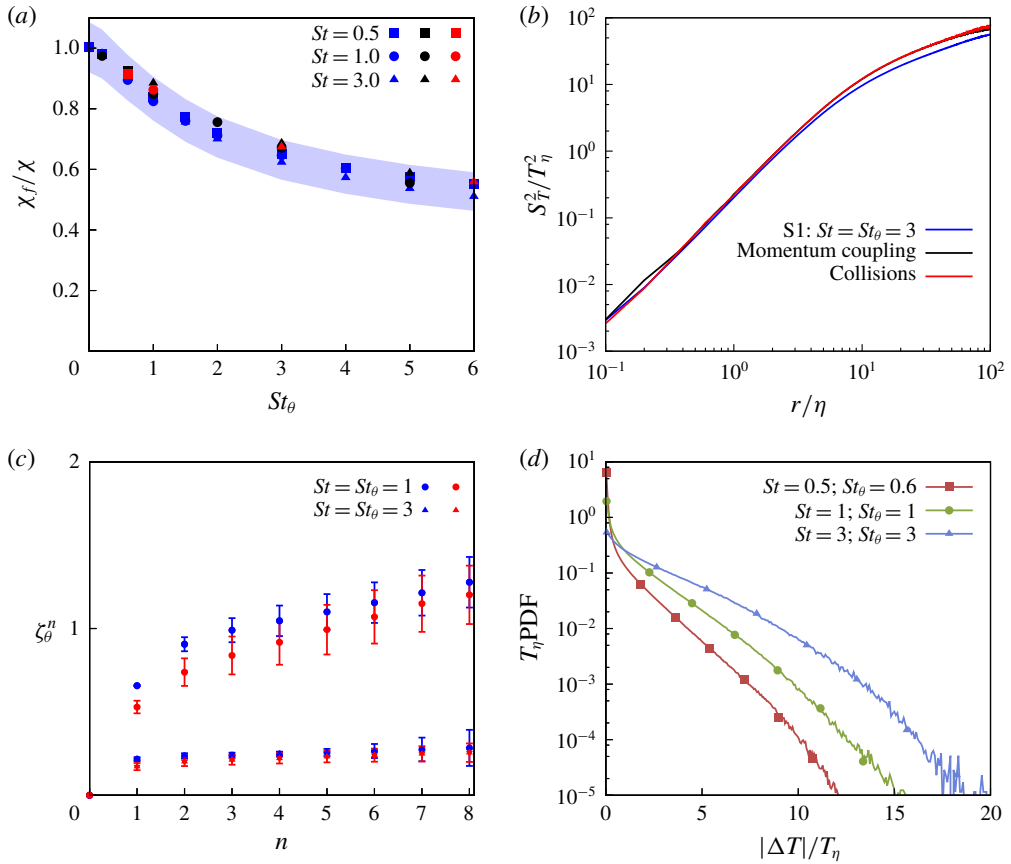
FIGURE 17. (Colour online) (*a*) Dissipation rate χ_f of the fluid temperature fluctuations, for different St as a function of St_θ and (*b*) second-order fluid temperature structure function, at $St = St_\theta = 3$, with and without momentum coupling and elastic collisions. (*c*) Scaling exponents of the particle temperature structure functions at small separation, with and without elastic collisions and momentum two-way coupling. Blue colour indicates one-way momentum coupling and two-way temperature coupling, black colour indicates two-way momentum and temperature coupling and red colour indicates two-way momentum and temperature coupling with elastic collisions between particles. (*d*) PDF of the temperature difference between colliding particles. The Kolmogorov scale quantities are computed by using the overall dissipation rate.

Appendix B. Estimating the actual temperature field

The paper presented the statistics of the carrier temperature field $T(\mathbf{x}, t)$, which can be resolved on the computational grid, within the limits of the point-particle model. In that model, both the particle size and the region perturbed by the particle are assumed to be much smaller than the Kolmogorov scale. The near-particle field changes are excluded in the carrier resolved fluid temperature field, which is an approximation of the actual temperature field far from particles. On the other hand, the actual temperature field includes the near-particle field perturbations, which vary on scales smaller than the Kolmogorov scale, down to the particle size, and it is such that the actual fluid temperature matches the particle temperature at the particle surface

(that is, there is no thermal slip). The carrier temperature field can be understood as the actual temperature field filtered at the computational grid resolution scale, that is comparable with the Kolmogorov length scale and much larger than the particle size. Since large temperature gradients can be expected in the perturbed regions, which are not explicitly accounted for by the carrier temperature field, in this appendix we analyse how the statistics of the actual temperature field relate to the particle temperature and resolved temperature field statistics.

B.1. *Moments of the actual temperature gradient*

Let us call T_* the actual temperature field, which is given by the sum of the carrier field $T(\boldsymbol{x}, t)$ (that is the one considered throughout the paper) and by the perturbations, $\tilde{T}_p(\boldsymbol{x}, t)$, induced by the particles. The carrier field has variations on a spatial and temporal scale from the integral scale down to the Kolmogorov microscale, while the perturbation variations are all concentrated around the particles, in a volume with a size proportional to their radius r_p. In the dilute regime we are considering, the perturbation fields induced by each particle do not overlap. Also, the suspended particles are small enough so that the Reynolds number of the relative motion with respect to the carrier fluid is small. Therefore the enthalpy equation around each particle reduces to the Fourier equation,

$$\frac{\partial T_*}{\partial t} = \kappa \nabla^2 T_*, \tag{B 1}$$

with the following boundary conditions,

$$\|\boldsymbol{x} - \boldsymbol{x}_p\| = r_p \quad \Rightarrow \quad T_* = \theta_p, \tag{B 2}$$

$$\|\boldsymbol{x} - \boldsymbol{x}_p\| \to +\infty \quad \Rightarrow \quad T_* \to T. \tag{B 3}$$

Equation (B 1) gives the perturbed temperature field around the particle in a particle-centred frame. Since particles have sub-Kolmogorov size, $r_p \ll \eta$, and the Prandtl number is unitary in our simulations, T can be considered uniform on the particle scale. The time scale of heat diffusion τ_d is much shorter than the time scale of the fastest fluctuations of the carrier temperature field T, which is of the order of the Kolmogorov time scale τ_η and $\tau_d/\tau_\eta \sim (r_p/\eta)^2 \ll 1$. Therefore, the solution of (B 1) with boundary conditions (B 3) around each particle can be approximated by its quasi-steady solution so that the actual temperature field is

$$T_*(\boldsymbol{x}, t) = T(\boldsymbol{x}, t) + \sum_{p=1}^{N_P} (\theta_p - T(\boldsymbol{x}_p, t)) \frac{r_p}{\|\boldsymbol{x} - \boldsymbol{x}_p\|} \tag{B 4}$$

and its gradient reads

$$\nabla T_* = \nabla T - \sum_{p=1}^{N_P} (\theta_p - T(\boldsymbol{x}_p)) \frac{r_p}{\|\boldsymbol{x} - \boldsymbol{x}_p\|^3} (\boldsymbol{x} - \boldsymbol{x}_p). \tag{B 5}$$

Equation (B 5) is the basis to derive the point-particle closure of the particle heat flux, equation (2.3*c*) and, as we will show, it also allows to recover the single-point moments of the actual temperature gradient, which is the superposition of the carrier

temperature gradient and the disturbance induced by the particles. Since the flow is statistically homogeneous, we may replace statistical averages with spatial averages. Let us indicate with Ω the overall domain, with Ω_p the region occupied by the pth particle and $\Omega_f = \Omega - \cup_p \Omega_p$ the region occupied by the fluid. The volume of the region occupied by the fluid is $|\Omega_f| = |\Omega|(1 - \phi)$ where $\phi = \sum_p |\Omega_p|/|\Omega|$ is the particle volume fraction. Since particles are very small with respect to the scale of spatial variation of the carrier temperature field, the disturbance induced by the particle is non-negligible only in a small region surrounding the particle. Let us indicate the perturbed volume around each particle by $\tilde{\Omega}_p$, a ball of radius αr_p, where r_p is the particle radius and $\alpha > 1$ indicates to how many radii far from the particle the disturbance on the temperature gradient becomes negligible. A one-dimensional sketch of the point-particle model under consideration is in figure 18(*a*). In the undisturbed fluid volume $\tilde{\Omega}_f = \Omega - \cup_p \tilde{\Omega}_p$ the particle perturbations are negligible and the actual temperature is given only by the carrier temperature field. On the other hand, in the perturbed region, the actual temperature is the sum of the resolved and disturbance temperature. Therefore we have,

$$T_*(\boldsymbol{x}, t) = T(\boldsymbol{x}, t), \quad \boldsymbol{x} \in \tilde{\Omega}_f \quad T_*(\boldsymbol{x}, t) = T(\boldsymbol{x}, t) + \tilde{T}_p(\boldsymbol{x}, t), \quad \boldsymbol{x} \in \tilde{\Omega}_p, \quad \text{(B 6a,b)}$$

where $\tilde{T}_p = (\theta_p - T(\boldsymbol{x}_p, t))r_p/\|\boldsymbol{x} - \boldsymbol{x}_p\|$ according to (B 4). The nth-order moment of the actual temperature gradient may be then evaluated by spatial average,

$$\langle \|\boldsymbol{\nabla} T_*\|^n \rangle = \frac{1}{|\Omega|} \int_{\tilde{\Omega}_f} (\|\boldsymbol{\nabla} T\|^2)^{n/2} \, \mathrm{d}\boldsymbol{x} + \frac{1}{|\Omega|} \sum_p \int_{\tilde{\Omega}_p} (\|\boldsymbol{\nabla} T_*\|^2)^{n/2} \, \mathrm{d}\boldsymbol{x}. \quad \text{(B 7)}$$

In the region perturbed by the particle, the gradient of the disturbance field is larger than the gradient of the carrier field, since the disturbance decays fast in a region which is tiny with respect to the Kolmogorov scale. Therefore, using $\|\boldsymbol{\nabla} T\| \ll \|\boldsymbol{\nabla} \tilde{T}_p\|$, the temperature field can be Taylor expanded in the perturbed regions, retaining terms up to $(\|\boldsymbol{\nabla} T\|/\|\boldsymbol{\nabla} \tilde{T}_p\|)^2$,

$$\|\boldsymbol{\nabla} T_*\|^n \sim \|\boldsymbol{\nabla} \tilde{T}_p\|^n \left[1 + n \frac{\boldsymbol{\nabla} T \cdot \boldsymbol{\nabla} \tilde{T}_p}{\|\boldsymbol{\nabla} \tilde{T}_p\|^2} + \frac{n}{2} \frac{\|\boldsymbol{\nabla} T\|^2}{\|\boldsymbol{\nabla} \tilde{T}_p\|^2} + \frac{n(n-2)}{2} \frac{(\boldsymbol{\nabla} T \cdot \boldsymbol{\nabla} \tilde{T}_p)^2}{\|\boldsymbol{\nabla} \tilde{T}_p\|^4} \right]. \quad \text{(B 8)}$$

The last term on the right-hand side of (B 8) can be estimated by using the Schwarz inequality to obtain

$$\|\boldsymbol{\nabla} T_*\|^n \lesssim \|\boldsymbol{\nabla} \tilde{T}_p\|^n + n\boldsymbol{\nabla} T \cdot \boldsymbol{\nabla} \tilde{T}_p \|\boldsymbol{\nabla} \tilde{T}_p\|^{n-2} + \frac{n(n-1)}{2} \|\boldsymbol{\nabla} T\|^2 \|\boldsymbol{\nabla} \tilde{T}_p\|^{n-2}. \quad \text{(B 9)}$$

Equation (B 9) provides a local upper bound for powers of the actual temperature gradient in the perturbed region (while $\boldsymbol{\nabla} T_* = \boldsymbol{\nabla} T$ in the unperturbed region), which allows us to compute an upper bound for the moments of the actual temperature gradient. Using (B 9) in (B 7) leads to

$$\langle \|\boldsymbol{\nabla} T_*\|^n \rangle \lesssim \frac{1}{|\Omega|} \int_{\tilde{\Omega}_f} \|\boldsymbol{\nabla} T\|^n \, \mathrm{d}\boldsymbol{y} + \frac{1}{|\Omega|} \sum_p \int_{\tilde{\Omega}_p} [n\boldsymbol{\nabla} T \cdot \boldsymbol{\nabla} \tilde{T}_p \|\boldsymbol{\nabla} \tilde{T}_p\|^{n-2}$$
$$+ \|\boldsymbol{\nabla} \tilde{T}_p\|^n + \frac{n(n-1)}{2} \|\boldsymbol{\nabla} T\|^2 \|\boldsymbol{\nabla} \tilde{T}_p\|^{n-2}] \, \mathrm{d}\boldsymbol{y}_p. \quad \text{(B 10)}$$
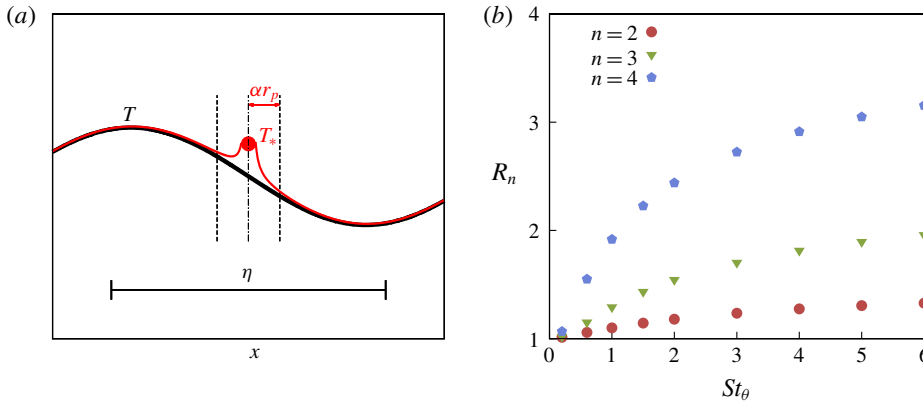
FIGURE 18. (Colour online) (*a*) Sketch of the particle model. The sizes of the particle and of the perturbed region are out of proportion for the sake of clarity. (*b*) Ratio between the nth-order moment of the actual temperature gradient and the resolved carrier temperature gradient, $R_n = (\langle \|\nabla T_*\|^n\rangle / \langle \|\nabla T\|^n\rangle)^{1/n}$, as a function of the particle thermal inertia at $St=1$.

The average of the product of the carrier field and the disturbance is negligible, since the carrier field varies on scale η and can be considered constant on scale $\alpha r_p \ll \eta$, except in small regions of the domain in which extreme field temperature gradients take place,

$$\int_{\tilde{\Omega}_p} \nabla T \cdot \nabla \tilde{T}_p \|\nabla \tilde{T}_p\|^{n-2} \, \mathrm{d}\mathbf{y}_p$$
$$\simeq (T(\mathbf{x}_p, t) - \theta_p)|T(\mathbf{x}_p, t) - \theta_p|^{n-2} r_p^{n-1} \nabla T(\mathbf{x}_p, t) \cdot \int_{\tilde{\Omega}_p} \mathbf{y}_p \|\mathbf{y}_p\|^{1-2n} \, \mathrm{d}\mathbf{y}_p = 0, \quad \text{(B 11)}$$

where $\mathbf{y}_p = \mathbf{x} - \mathbf{x}_p$ and the spherical symmetry of the perturbation has been used. Computing the integrals involving $\tilde{T}_p$ in (B 10), an upper bound for the nth-order moment of the actual fluid temperature gradient is obtained

$$\langle \|\nabla T_*\|^n\rangle \lesssim (1 - \alpha^3\phi)\langle \|\nabla T\|^n\rangle + \phi \frac{3}{2n-3}(1 - \alpha^{3-2n}) \left\langle \left| \frac{\theta_p - T(\mathbf{x}_p, t)}{r_p} \right|^n \right\rangle$$
$$+ \phi \frac{3n(n-1)}{4n-14}(1 - \alpha^{7-2n}) \left\langle \|\nabla T(\mathbf{x}_p, t)\|^2 \left| \frac{\theta_p - T(\mathbf{x}_p, t)}{r_p} \right|^{n-2} \right\rangle. \quad \text{(B 12)}$$

Regarding the corrections due to α, equation (B 5) shows that the disturbance temperature gradient decays within a few radii from the particle. We may assume α large but still $\alpha r_p \ll \eta$ because of the marked scale separation hypothesis between the particle size and the Kolmogorov length scale, $r_p \ll \eta$. By hypothesis $\alpha^3\phi \ll 1$ and, therefore, also $\alpha^{7-2n}\phi \ll 1$ for $n \geqslant 2$.

The first term on the right-hand side of (B 12) is the contribution of the carrier flow, the other two terms are the contribution of the local perturbation due to the particles. The inequality in (B 12) is only due to the last term, which has been overestimated by the Schwarz inequality. The relative importance of the terms in (B 12) is now estimated in order to obtain a direct estimation instead of an upper bound for the

moments of the actual temperature gradient. We exploit the fact that the disturbance gradient is much larger and more intermittent than the resolved gradient, therefore the second term in (B 12), which behaves as $|(\theta_p - T(\boldsymbol{x}_p, t))/r_p|^n$, is dominant with respect the third term in the same equation, that behaves only as $|(\theta_p - T(\boldsymbol{x}_p, t))/r_p|^{n-2}$. An estimation of the ratio between the order of magnitude of the third and second terms on the right-hand side of (B 12), that is,

$$\mathcal{C}_n = \frac{n(n-1)(2n-3)}{4n-14} \frac{1-\alpha^{7-2n}}{1-\alpha^{3-2n}} \frac{\langle \|\boldsymbol{\nabla} T(\boldsymbol{x}_p, t)\|^2 |\theta_p - T(\boldsymbol{x}_p, t)|^{n-2}\rangle}{\langle |\theta_p - T(\boldsymbol{x}_p, t)|^n\rangle} r_p^2, \qquad (\text{B 13})$$

can be obtained neglecting the coupling between the resolved and perturbation gradient, which is justified due to the wide scale separation of those two fields, and using the results in Bec *et al.* (2014), where it is shown that the average dissipation rate evaluated at the particle position is not larger than two times the overall dissipation rate. Therefore, the ratio between the order of magnitude of the third and second terms on the right-hand side of (B 12) can be estimated as

$$\mathcal{C}_n \lesssim \frac{6}{K_n} \frac{\chi_f}{\chi_p} \left| \frac{n(n-1)(2n-3)}{4n-14} \right| \max(1, \alpha^{7-2n})\phi, \qquad (\text{B 14})$$

where

$$K_n = \frac{\langle |\theta_p - T(\boldsymbol{x}_p, t)|^n\rangle}{\langle |\theta_p - T(\boldsymbol{x}_p, t)|^{n-2}\rangle \langle |\theta_p - T(\boldsymbol{x}_p, t)|^2\rangle} \qquad (\text{B 15})$$

and χ_f/χ_p depends on St_θ and weakly on St, as in figure 2(*b*). Since $\alpha^3\phi \ll 1$, as required by the two-way coupled point-particle model, and K_n is expected to be large for $n > 2$ due to the high intermittency of the disturbance gradient (e.g. $K_4 = O(10)$ from figure 3*f*), we expect that $\mathcal{C}_n \ll 1$ for moderate n (e.g. $n \leqslant 4$) and St_θ not too small (so that χ_f/χ_p not very large). The estimation in (B 14) can be rewritten using (B 13), (3.3) and (3.4) together with the definition of Kolmogorov scales, $\langle \|\boldsymbol{\nabla} T\|^2\rangle = T_\eta^2/\eta^2$, which gives

$$\mathcal{C}_n \lesssim \frac{2}{K_n} \left| \frac{n(n-1)(2n-3)}{4n-14} \right| \max(1, \alpha^{7-2n}) \frac{T_\eta^2}{\langle |\theta_p - T(\boldsymbol{x}_p, t)|^2\rangle} \left(\frac{r_p}{\eta} \right)^2. \qquad (\text{B 16})$$

Therefore $\mathcal{C}_n \ll 1$ for small particles, moderate n and St_θ reasonably large (that is, $|\theta_p - T(\boldsymbol{x}_p, t)|/T_\eta$ not very small). Both estimations, equations (B 14) and (B 16), show that the second term on the right-hand side of (B 12) is the leading term of the contribution of the particle perturbation to the actual temperature gradient moments, while the third term on the right-hand side of (B 12) is sub-leading, for moderate n (e.g. $n \leqslant 4$), $\phi \ll 1$ and $r_p/\eta \ll 1$, which are basic hypotheses of the point-particle model. Therefore, the following simplified estimation for the moments of the actual temperature field is obtained:

$$\langle \|\boldsymbol{\nabla} T_*\|^n\rangle \sim \langle \|\boldsymbol{\nabla} T\|^n\rangle + \frac{3\phi}{2n-3} \left\langle \left| \frac{\theta_p - T(\boldsymbol{x}_p, t)}{r_p} \right|^n \right\rangle, \quad n \geqslant 2. \qquad (\text{B 17})$$

Equation (B 17) with $n = 2$ is the balance of thermal dissipation rate, that is (3.2), derived in the paper from the carrier flow temperature field equation (2.1*c*), which includes the particle thermal feedback. The only hypotheses necessary to obtain equation (B 17) are those that are also assumed for the validity of the point-particle

model, without the need for any *ad hoc* assumption. It is worth noting that the contribution of the particle perturbation to the actual temperature gradient moments can become dominant with respect to the carrier temperature field contribution. Indeed, the ratio between the second and first terms on right-hand side of (B 17) can be roughly estimated to be proportional to $\phi(\eta/r_p)^n$, which shows that the particle perturbation contribution dominates for large n, since in the point-particle model hypothesis $\phi \ll 1$ but $\eta/r_p \gg 1$. This is a signature of the intermittency introduced by the perturbation due to the particles. The quantity

$$R_n = \left(\frac{\langle \|\boldsymbol{\nabla} T_*\|^n \rangle}{\langle \|\boldsymbol{\nabla} T\|^n \rangle} \right)^{1/n} \tag{B 18}$$

can be used to measure the overall contribution of the perturbed regions to the temperature gradient moments, and it is shown in figure 18(*b*) as a function of the thermal Stokes number, for $n \leqslant 4$ and $St = 1$. As expected, for small particle thermal inertia $R_n \sim 1$ and the difference between the actual temperature gradient distribution and the resolved temperature gradient distribution increases with St_θ. The actual temperature gradient $\boldsymbol{\nabla} T_*$ is more intermittent than the carrier flow temperature gradient $\boldsymbol{\nabla} T$ (which does not include the particle disturbance) discussed in the paper. The high-order moments of the actual temperature gradient might be even larger than the prediction in (B 17), since the weight of the term neglected in (B 12) is proportional to the order of the moment, n. The enhanced fluid flow intermittency due to the suspended particles is consistent with the results from particle-resolved direct numerical simulations of turbulent flows laden with small fixed spheres (Vreman 2016).

B.2. *Actual temperature field PDF*

The PDF of the actual temperature field T_* can be obtained from the PDF of the carrier temperature field T and the PDF of the particle temperature through equation (B 4). A simple estimation, which overestimates the difference between the PDFs of T and T_*, can be obtained by assuming that T_* is equal to the particle temperature θ_p within $\tilde{\Omega}_p$,

$$T_*(\boldsymbol{x}, t) = T(\boldsymbol{x}, t), \boldsymbol{x} \in \tilde{\Omega}_f \quad T_*(\boldsymbol{x}, t) \approx \theta_p, \boldsymbol{x} \in \tilde{\Omega}_p. \tag{B 19a,b}$$

The PDF of the actual temperature field is given by,

$$\rho_{T_*}(T') = \rho(T' \text{ and } \boldsymbol{x} \in \tilde{\Omega}_f) + \rho(T' \text{ and } \boldsymbol{x} \in \cup_p \tilde{\Omega}_p), \tag{B 20}$$

and, through (B 19), it reduces to

$$\begin{aligned} \rho_{T_*}(T') &= (1 - \alpha^3 \phi)\rho_T(T') + \alpha^3 \phi \rho_\theta(T') \\ &= \rho_T(T') + \alpha^3 \phi(\rho_\theta(T') - \rho_T(T')). \end{aligned} \tag{B 21}$$

Since $\alpha^3 \phi \ll 1$ and the difference between the distribution of θ_p and T is moderate (see figures 5 and 6), the difference between the carrier temperature distribution T and the actual temperature distribution T_* is negligible and $\rho_T \sim \rho_{T_*}$.

B.3. *Structure functions*

The moments of the actual temperature gradient provide information about the temperature structure functions at small separation. Indeed, $\Delta T_*(r) \sim \nabla T_* \cdot r$ for $r \to 0$ and the overall thermal dissipation rate χ, which is imposed by the forcing, is due to the gradients of the actual fluid temperature field,

$$\chi = \kappa \langle \|\nabla T_*\|^2 \rangle. \tag{B 22}$$

Therefore, invoking isotropy, the actual temperature field second-order structure function at small separation is

$$S_{T_*}^2(r) \sim \left\langle \frac{\partial T_*}{\partial x_i} \frac{\partial T_*}{\partial x_j} \right\rangle r_i r_j = \langle \|\nabla T_*\|^2 \rangle \frac{r^2}{3} = \frac{r^2 \chi}{3\kappa}, \quad r \to 0, \tag{B 23}$$

while the second-order structure function of the carrier temperature field is $\sim r^2 \chi_f/(3\kappa)$ at small separation. Small deviations from this limit may occur due to lack of isotropy in the immediate vicinity of the particle. The structure function of the actual temperature field at small separation is proportional to the overall thermal dissipation rate. This again reflects the fact that physically all the dissipation rate derives from the actual fluid temperature gradient, the thermal slip $|\theta_p - T(x_p, t)|$ being only an artefact of the point-particle model. In this work, the overall thermal dissipation rate χ is the same for all the simulations, therefore the structure function of the actual temperature field at small separation is the same for each St and St_θ. On the other hand at large separation,

$$S_{T_*}^2(r) \sim 2\langle T_*^2 \rangle, \quad r \gg \ell_*, \tag{B 24}$$

where ℓ_* is the correlation length of the actual temperature field. Information about the structure function can be then extrapolated by analysing the single-point actual temperature field statistics. For these one-point statistics, however, the modification due to the particles is expected to be small, as in §B.2. In conclusion, the variation of the fluid temperature structure function S_T at small separation due to the near-particle field changes is expected to be pronounced, while the effect of the near-particle field on the fluid temperature structure functions at large separation is expected to be very moderate in the dilute regime.

REFERENCES

BEC, J., BIFERALE, L., CENCINI, M., LANOTTE, A., MUSACCHIO, S. & TOSCHI, F. 2007 Heavy particle concentration in turbulence at dissipative and inertial scales. *Phys. Rev. Lett.* **98**, 084502.

BEC, J., HOMANN, H. & KRSTULOVIC, G. 2014 Clustering, fronts, and heat transfer in turbulent suspensions of heavy particles. *Phys. Rev. Lett.* **112**, 234503.

BEYLKIN, G. 1995 On the fast fourier transform of functions with singularities. *Appl. Comput. Harmon. Anal.* **2** (4), 363–381.

BOIVIN, M., SIMONIN, O. & SQUIRES, K. D. 1998 Direct numerical simulation of turbulence modulation by particles in isotropic turbulence. *J. Fluid Mech.* **375**, 235–263.

BOTTO, L. & PROSPERETTI, A. 2012 A fully resolved numerical simulation of turbulent flow past one or several spherical particles. *Phys. Fluids* **24** (1), 013303.

BRAGG, A. D. & COLLINS, L. R. 2014a New insights from comparing statistical theories for inertial particles in turbulence: I. Spatial distribution of particles. *New J. Phys.* **16**, 055013.

BRAGG, A. D. & COLLINS, L. R. 2014*b* New insights from comparing statistical theories for inertial particles in turbulence: II. Relative velocities of particles. *New J. Phys.* **16**, 055014.

BRAGG, A. D., IRELAND, P. J. & COLLINS, L. R. 2015*a* Mechanisms for the clustering of inertial particles in the inertial range of isotropic turbulence. *Phys. Rev.* E **92**, 023029.

BRAGG, A. D., IRELAND, P. J. & COLLINS, L. R. 2015*b* On the relationship between the non-local clustering mechanism and preferential concentration. *J. Fluid Mech.* **780**, 327–343.

CANUTO, C., HUSSAINI, M. Y., QUARTERONI, A. & ZANG, T. A. 1988 *Spectral Methods in Fluid Mechanics*. Springer.

CARBONE, M. & IOVIENO, M. 2018 Application of the non-uniform fast Fourier transform to the direct numerical simulation of two-way coupled turbulent flows. *WIT Trans. Engng Sci.* **120**, 237–248.

CELANI, A., LANOTTE, A., MAZZINO, A. & VERGASSOLA, M. 2000 Universality and saturation of intermittency in passive scalar turbulence. *Phys. Rev. Lett.* **84**, 2385–2388.

CHUN, J., KOCH, D. L., RANI, S., AHLUWALIA, A. & COLLINS, L. R. 2005 Clustering of aerosol particles in isotropic turbulence. *J. Fluid Mech.* **536**, 219–251.

DAS, S. K., CHOI, S. U. S. & PATEL, H. E. 2006 Heat transfer in nanofluids – a review. *Heat Transfer Engng* **27** (10), 3–19.

DE LILLO, F., CENCINI, M., DURHAM, W. M., BARRY, M., STOCKER, R., CLIMENT, E. & BOFFETTA, G. 2014 Turbulent fluid acceleration generates clusters of gyrotactic microorganisms. *Phys. Rev. Lett.* **112**, 044502.

DHARIWAL, R. & RANI, S. L. 2018 Effects of deterministic and stochastic forcing schemes on the relative motion of inertial particles in DNS of isotropic turbulence. *Powder Technol.* **339**, 46–69.

ELGHOBASHI, S. 1991 Particle-laden turbulent flows: direct simulation and closure models. *Appl. Sci. Res.* **48** (3), 301–314.

ELGHOBASHI, S. 1994 On predicting particle-laden turbulent flows. *Appl. Sci. Res.* **52** (4), 309–329.

GOTOH, T. & WATANABE, T. 2015 Power and nonpower laws of passive scalar moments convected by isotropic turbulence. *Phys. Rev. Lett.* **115**, 114502.

GÖTZFRIED, P., KUMAR, B., SHAW, R. A. & SCHUMACHER, J. 2017 Droplet dynamics and fine-scale structure in a shearless turbulent mixing layer with phase changes. *J. Fluid Mech.* **814**, 452–483.

GRABOWSKI, W. W. & WANG, L. P. 2013 Growth of cloud droplets in a turbulent environment. *Annu. Rev. Fluid Mech.* **45** (1), 293–324.

GUALTIERI, P., PICANO, F., SARDINA, G. & CASCIOLA, C. M. 2013 Clustering and turbulence modulation in particle-laden shear flows. *J. Fluid Mech.* **715**, 134–162.

GUALTIERI, P., PICANO, F., SARDINA, G. & CASCIOLA, C. M. 2015 Exact regularized point particle method for multiphase flows in the two-way coupling regime. *J. Fluid Mech.* **773**, 520–561.

GUSTAVSSON, K. & MEHLIG, B. 2011 Ergodic and non-ergodic clustering of inertial particles. *Eur. Phys. Lett.* **96**, 60012.

GUSTAVSSON, K. & MEHLIG, B. 2016 Statistical models for spatial patterns of heavy particles in turbulence. *Adv. Phys.* **65** (1), 1–57.

VAN HINSBERG, M. A. T., TEN THIJE BOONKKAMP, J. H. M., TOSCHI, F. & CLERCX, H. J. H. 2012 On the efficiency and accuracy of interpolation methods for spectral codes. *SIAM J. Sci. Comput.* **34** (4), B479–B498.

HOCHBRUCK, M. & OSTERMANN, A. 2010 Exponential integrators. *Acta Numerica* **19**, 209–286.

HOLZER, M. & SIGGIA, E. D. 1994 Turbulent mixing of a passive scalar. *Phys. Fluids* **6** (5), 1820–1837.

HORWITZ, J. A. K. & MANI, A. 2016 Accurate calculation of Stokes drag for point-particle tracking in two-way coupled flows. *J. Comput. Phys.* **318**, 85–109.

IRELAND, P. J., BRAGG, A. D. & COLLINS, L. R. 2016*a* The effect of Reynolds number on inertial particle dynamics in isotropic turbulence. Part 1. Simulations without gravitational effects. *J. Fluid Mech.* **796**, 617–658.

IRELAND, P. J., BRAGG, A. D. & COLLINS, L. R. 2016*b* The effect of Reynolds number on inertial particle dynamics in isotropic turbulence. Part 2. Simulations with gravitational effects. *J. Fluid Mech.* **796**, 659–711.

KRAICHNAN, R. H. 1994 Anomalous scaling of a randomly advected passive scalar. *Phys. Rev. Lett.* **72**, 1016–1019.

KUERTEN, J. G. M. 2016 Point-particle DNS and LES of particle-laden turbulent flow – a state-of-the-art review. *Flow Turbul. Combust.* **97** (3), 689–713.

KUERTEN, J. G. M., VAN DER GELD, C. W. M. & GEURTS, B. J. 2011 Turbulence modification and heat transfer enhancement by inertial particles in turbulent channel flow. *Phys. Fluids* **23** (12), 123301.

KUMAR, B., SCHUMACHER, J. & SHAW, R. A. 2013 Cloud microphysical effects of turbulent mixing and entrainment. *Theor. Comput. Fluid Dyn.* **27**, 361–376.

KUMAR, B., SCHUMACHER, J. & SHAW, R. A. 2014 Lagrangian mixing dynamics at the cloudy-clear air interface. *J. Atmos. Sci.* **71** (7), 2564–2580.

MAXEY, M. R. 1987 The gravitational settling of aerosol particles in homogeneous turbulence and random flow fields. *J. Fluid Mech.* **174**, 441–465.

MAXEY, M. R. & RILEY, J. 1983 Equation of motion for a small rigid sphere in a nonuniform flow. *Phys. Fluids* **26** (4), 883–889.

MOMENIFAR, M. R., AKHAVAN-BEHABADI, M. A., NASR, M. & HANAFIZADEH, P. 2015 Effect of lubricating oil on flow boiling characteristics of R-600a/oil inside a horizontal smooth tube. *Appl. Therm. Engng* **91**, 62–72.

ONISHI, R., TAKAHASHI, K. & VASSILICOS, J. C. 2013 An efficient parallel simulation of interacting inertial particles in homogeneous isotropic turbulence. *J. Comput. Phys.* **242**, 809–827.

OVERHOLT, M. R. & POPE, S. B. 1996 Direct numerical simulation of a passive scalar with imposed mean gradient in isotropic turbulence. *Phys. Fluids* **8** (11), 3128–3148.

PEKUROVSKY, D. 2012 P3DFFT: a framework for parallel computations of Fourier transforms in three dimensions. *SIAM J. Sci. Comput.* **34** (4), C192–C209.

PRASHER, R., EVANS, W., MEAKIN, P., FISH, J., PHELAN, P. & KEBLINSKI, P. 2006 Effect of aggregation on thermal conduction in colloidal nanofluids. *Appl. Phys. Lett.* **89** (14), 143119.

PRUPPACHER, H. R. & KLETT, J. D. 2010 *Microphysics of Clouds and Precipitation*. Springer Netherlands.

SALAZAR, J. P. L. C. & COLLINS, L. R. 2012 Inertial particle relative velocity statistics in homogeneous isotropic turbulence. *J. Fluid Mech.* **696**, 45–66.

SHRAIMAN, B. I. & SIGGIA, E. D. 2000 Scalar turbulence. *Nature* **405**, 639–646.

SREENIVASAN, K. R. 1996 The passive scalar spectrum and the Obukhov–Corrsin constant. *Phys. Fluids* **8** (1), 189–196.

SUNDARAM, S. & COLLINS, L. R. 1996 Numerical considerations in simulating a turbulent suspension of finite-volume particles. *J. Comput. Phys.* **124** (2), 337–350.

TAKEUCHI, T. & LIN, D. N. C. 2002 Radial flow of dust particles in accretion disks. *Astrophys. J.* **581** (2), 1344.

TAYLOR, G. I. 1922 Diffusion by continuous movements. *Proc. Lond. Math. Soc.* **s2–20** (1), 196–212.

TOSCHI, F. & BODENSCHATZ, E. 2009 Lagrangian properties of particles in turbulence. *Annu. Rev. Fluid Mech.* **41** (1), 375–404.

TOWNS, J., COCKERILL, T., DAHAN, M., FOSTER, I., GAITHER, K., GRIMSHAW, A., HAZLEWOOD, V., LATHROP, S., LIFKA, D., PETERSON, G. D. *et al.* 2014 Xsede: accelerating scientific discovery. *Comput. Sci. Engng* **16** (5), 62–74.

VOSSKUHLE, M., PUMIR, A., LÉVÊQUE, E. & WILKINSON, M. 2014 Prevalence of the sling effect for enhancing collision rates in turbulent suspensions. *J. Fluid Mech.* **749**, 841–852.

VREMAN, A. W. 2016 Particle-resolved direct numerical simulation of homogeneous isotropic turbulence modified by small fixed spheres. *J. Fluid Mech.* **796**, 40–85.

WANG, L. P. & MAXEY, M. R. 1993 Settling velocity and concentration distribution of heavy particles in homogeneous isotropic turbulence. *J. Fluid Mech.* **256**, 27–68.

WARHAFT, Z. 2000 Passive scalars in turbulent flows. *Annu. Rev. Fluid Mech.* **32** (1), 203–240.

WATANABE, T. & GOTOH, T. 2004 Statistics of a passive scalar in homogeneous turbulence. *New J. Phys.* **6** (1), 40.

WILKINSON, M. & MEHLIG, B. 2005 Caustics in turbulent aerosols. *Europhys. Lett.* **71** (2), 186–192.

ZAICHIK, L., ALIPCHENKOV, V. M. & SINAISKI, E. G. 2009 *Particles in Turbulent Flows*, vol. 84. Wiley.

ZAMANSKY, R., COLETTI, F., MASSOT, M. & MANI, A. 2014 Radiation induces turbulence in particle-laden fluids. *Phys. Fluids* **26** (7), 071701.

ZAMANSKY, R., COLETTI, F., MASSOT, M. & MANI, A. 2016 Turbulent thermal convection driven by heated inertial particles. *J. Fluid Mech.* **809**, 390–437.

ZONTA, F., MARCHIOLI, C. & SOLDATI, A. 2008 Direct numerical simulation of turbulent heat transfer modulation in micro-dispersed channel flow. *Acta Mech.* **195** (1–4), 305–326.

ZORZETTO, E., BRAGG, A. D. & KATUL, G. 2018 Extremes, intermittency, and time directionality of atmospheric turbulence at the crossover from production to inertial scales. *Phys. Rev. Fluids* **3**, 094604.